Time-resolved imaging and analysis of the electron beam-induced formation of an open-cage metallo-azafullerene

Helen Hoelzel,[3,5] Sol Lee,[1] Konstantin Yu. Amsharov,[6] Norbert Jux,[5] Koji Harano,[3,4] Eiichi Nakamura,[3] Dominik Lungerich,[1,2,3]*

[1] Center for Nanomedicine (CNM), Institute for Basic Science (IBS), IBS Hall, 50 Yonsei-ro, Seodaemun-gu, Seoul, 03722, South Korea.

[2] Graduate Program of Nano Biomedical Engineering (NanoBME), Advanced Science Institute, Yonsei University, Seoul, 03722, South Korea.

[3] Department of Chemistry, The University of Tokyo, 7-3-1 Hongo, Bunkyo-ku, Tokyo 113-0033, Japan.

[4] Research Center for Advanced Measurement and Characterization, National Institute for Materials Science, 1-1 Namiki, Tsukuba 305-0044, Japan.

[5] Department of Chemistry and Pharmacy, Organic Chemistry II, Friedrich-Alexander-University Erlangen-Nuernberg (FAU), Nikolaus-Fiebiger-Str. 10, 91058, Erlangen, Germany.

[6] Department of Chemistry, Martin-Luther-University Halle-Wittenberg, Kurt-Mothes-Str. 2, 06120 Halle, Germany.

Email: d.lungerich@yonsei.ac.kr

Abstract: The bottom-up synthesis of strained hollow cage structures, such as fullerenes, using traditional thermal or photochemical methods remains one of the most challenging tasks in organic chemistry. Here, we demonstrate the synthetic use of an electron beam by in-depth single-molecule atomic resolution time-resolved transmission electron microscopy studies to induce the formation of an elusive doubly-holed fullerene-porphyrin cage structure from a well-defined benzoporphyrin precursor deposited on graphene. Through real-time imaging, we analyze the hybrid's peculiar ability to host up to two Pb atoms and subsequently gain insights into the dynamics of the Pb–Pb binding motif in this exotic metallo-organic cage structure. Through density functional theory calculations and image simulations, we conclude that the much slower secondary electrons, which accumulate in the irradiated area's periphery, can also initiate chemical reactions. Consequently, designing advanced carbon nanostructures by e-beam lithography will depend on the understanding and limitations of molecular radiation chemistry.

Keywords: molecular imaging; radiation chemistry; cinematic chemistry; single-molecule dynamics; DFT-modeling; transmission electron microscopy.

Technological advancements in high-resolution transmission electron microscopy (HRTEM) enabled single-molecule atomic-resolution time-resolved electron microscopy (SMART-EM)[1] or "*Chem*TEM" [2] techniques to literally change the chemists' view on molecular processes in real space and real-time analyses. A few recent highlights are the visualization and study of the NaCl nucleus emergence,[3] the prenucleation of MOF-2 and MOF-5,[4] the imaging of daptomycin molecules with and without calcium ions,[5] the bond-dissociation of HF and H_2O molecules in endohedral fullerenes,[6] the unsupported metal-metal bond in a Re_2 molecule,[7] the reactivity of metal clusters and polyoxometalates,[8,9] as well as ordered molecular superstructures.[10–12] However, the magnificent potential to observe dynamic events at the smallest scale of matter, namely at the atomic and molecular level, comes at a price and is generally described as radiation damage.[13–15] Typical destructive mechanisms include the material's ionization and subsequent destructive transformations (radiolysis) and the homolytic displacement of atoms from the structure, which received sufficient kinetic energy from the e-beam (knock-on displacement). These destructive effects are highly dependent on the specimen itself and vary with the elemental composition, binding characteristics, and electronic structure; however, also the imaging conditions, such as the acceleration voltage, the electron flux and total dose, as well as the temperature settings will impact the lifetime of molecular intermediates during SMART-EM imaging critically.[16]

On the other hand, from meticulously carried out cinematographic analyses of single-molecule reactions, several constructive and now well-understood reaction mechanisms were identified to occur under the e-beam. Apart from the homolytic dissociation of C–H bonds into radical pairs ($C^{\bullet}$ and $H^{\bullet}$) followed by subsequent radical recombination chemistry,[6,17] the [2 + 2] cycloaddition reaction of fullerenes,[16,18] and the Stone-Wales rearrangement to, for instance, peanut-shaped C_{120} nanotubes, have been identified.[19] However, compared to the continuously growing repertoire of thermally, photochemically, or mechanically initiated organic reaction mechanisms developed in wet-chemical laboratories, only a little knowledge about the control and selectivity of e-beam-induced mechanisms has been accumulated so far.[1,2] Recently, we identified another reaction mechanism proceeding under the electron beam in the pre-programmed synthesis of fullerene C_{60}, namely the cyclodehydrogenation.[20] While this particular reaction was not achieved photochemically or thermally in solution, carried out under flash vacuum pyrolysis condition at 1000 ºC, the reaction outcome is regioselective.[21,22] Importantly, it is not the result of a

thermodynamically driven rearrangement of carbon atoms to fullerene C_{60}, as known from the arc-discharge synthesis of fullerenes from graphite.[23]

This study shows the *de novo* design and synthesis of a three-dimensional ν-conjugated molecular nanostructure, enabled through the e-beam-induced cyclodehydrogenation reaction in the TEM. As elucidated from cinematographic SMART-EM analyses, the designed lead(II)-containing benzoporphyrin precursor **1Pb**, is shown to selectively zip up the respective *fjord* and *cove* region C–C bonds to form a three-dimensional hollow cage structure, an open-cage azafullerene, and freely diffusing Pb-atoms found on the graphene surface can be incorporated into the structure; one Pb atom as part of the endohedral cavity and another one complexed by the porphyrin macrocycle of the carbon exoskeleton. Correlated with electron-dose corrected TEM simulations and density functional theory (DFT) calculations, we identified this exotic hybrid structure and several key intermediates during its formation and subsequently gained mechanistic insights into the e-beam-induced transformations on the molecular level.

Results and discussion

Design and synthesis. We envisioned using the electron beam as a synthetic and imaging tool to induce and observe the formation of a fullerene-porphyrin hybrid **FP** ($C_{100}H_4N_4$) *via* the e-beam-induced cyclodehydrogenation reaction. For that purpose, we designed and synthesized 2-pyrenyl substituted benzoporphyrin **1** ($C_{100}H_{54}N_4$) *via* modified Lindsey condensation conditions (Fig. 1a) from masked isoindole **2** and 2-formylpyrene **3**; thermal unmasking of the isoindole moieties gave **1** in 81% overall yield. **3** was obtained in 53% yield after a lithium-halogen exchange of 2-bromopyrene **4**, followed by formylation with DMF. To introduce a high-contrast metal atom, **1** was metalated to **1Pb** ($C_{100}H_{52}N_4Pb$) using $Pb(OAc)_2$ in DMF at elevated temperature. We chose Pb as the central metal for the following reasons: 1) It has a high *Z*-contrast in TEM imaging, which facilitates the SMART-EM observations; 2) Unlike catalytically active transition metals with comparable contrast properties, such as platinum,[24] Pb as a p-block element is unlikely to undergo C-H bond activation reactions or other C–C bond-forming reactions under the electron beam. The successful metalation is easily verified by absorption spectroscopy through the significant Soret and Q-bands shifts of the metalated benzoporphyrin (Fig. 1b), whereas the absorption characteristics of the pyrene moieties remain nearly unaffected.

As predicted by DFT calculations, a consecutive zipping-up of the pyrenyl substituents with the benzoporphyrin core,[25] the resulting eight five-membered rings in the framework lead to a distortion of the initial saddle structure of **1Pb** (C_{2v} symmetry) to a C_{4v} symmetrical onion-shaped sphere with two opposing entrances to the endohedral cavity (Fig. 1c). The structure of the open-cage atoms, including the complexed metal atom, follows the isolated pentagon rule (IPR) for fullerenes. However, the IPR conditions are not met upon closing the lower rim in **FP** to twelve pentagons through the substitution of the hydrogen atoms by a quaternary fenestrane-type carbon atom (Fig. 1d). The thermochemical analysis (Fig. 1e) at the density functional M06-2X/def2-TZVP//ωB97X-D/6-31G(d) level of theory reveals an increase in relative energy over the consecutive 24 cyclodehydrogenation steps to around 30.1 eV, which corresponds to an average $\backslash E$ per step of 1.25 eV. In comparison, this value is less than for forming fullerene C_{60} from truxene derivative $C_{60}H_{30}$, which requires around 1.4 eV per step (compare Extended Data Fig. 1).[20] Thus, from a thermochemical perspective, the precursor design appears reasonable.

Fig. 1. Experimental and computational approach to fullerophyrin FP. **a**, Wet-chemical synthesis of benzoporphyrin precursor **1Pb**. **b**, Absorption spectra of **1** and **1Pb** in CH_2Cl_2 at rt, spectra normalized to pyrene's p-band. **c**, Electron beam-induced cyclodehydrogenation to **FP**. Top and side view of the DFT geometry optimized structure of free-base **FP**. **d**, Hypothetical closure of the lower rim opening of **FP** with a quaternary carbon atom with a [5.5.5.5]fenestrane motif to give a non-IPR cage structure. **e**, Thermochemical analysis of the consecutive H_2 loss *via* cyclodehydrogenation of **1** to **FP**. Only isomers obtained from a zipper mechanism were considered (108 intermediates).

Sample preparation and general (S)TEM analysis. We drop-casted 10 µL of a 10^{-5} M solution of **1Pb** dissolved in THF on a dry-cleaned graphene-coated TEM grid, the excess solution was dabbed off, and the grid was dried in high vacuum (10^{-5} Pa) for 2 h before insertion into the TEM. Observations were carried out with an aberration-corrected TEM (JEM-ARM200F) at 303±5 K at magnifications of 1000k, equipped with a scintillator-based CMOS camera (Gatan OneView). The vacuum of the specimen chamber was constant at $1x10^{-5}$ Pa, the acceleration voltage was set to 80 kV, and the camera frame rate was kept at 2 fps. Traces of remaining volatiles were removed in the TEM by heating the grid to 473 K for 1 h before exposure to the electron beam. After scanning the graphene surface for viable candidates, we discovered a spherical structure attached to a graphene monolayer (GML) near an amorphous aggregate of Pb atoms, which served as a Pb-atom reservoir (Fig. 2a). Nearby, several single Pb-atoms were found to diffuse at the edge of the amorphous carbon layer. As shown in the high-angle annular dark-field scanning transmission electron microscopy (HAADF-STEM) images in Fig. 2b, the sizes of the Pb aggregates span from 2 to 25 nm while maintaining only minor crystalline character. Energy-dispersive X-ray spectroscopy (EDS) and mapping confirmed that the clusters consist of Pb atoms and are no other metal artifacts from sample preparation or the fabrication of the gold grid. On the other hand, the expected ν–ν stacks of pristine **1Pb**, demetalated **1**, or even immobilized structures *via* C–C bonds to graphene were not observed (Fig. 2c), since all molecules appeared to have reacted before being imaged by the primary beam electrons (*vide infra*).

The sheer number of single Pb-atoms and aggregates is astonishing. However, it can be rationalized by a hot electron ($E_{kin} > 0$ eV) reduction mechanism,[26,27] as described in Fig. 2c: An electron attachment to **1Pb** occurs through secondary electrons ($E_{kin} << 50$ eV)[28] from the specimen in the outer periphery of the electron beam-irradiated area, herein defined as beam shadow. Then, the metal ion is quickly released (order of picoseconds) from the macrocycle onto the substrate *via* an electrochemical reduction of $\mathbf{1Pb}^0$ to $\mathbf{1Pb}^{-1}$ or $\mathbf{1Pb}^{-2}$. Albeit a less common technique, wet-chemical reductive demetallation of porphyrins has been reported in the literature.[29,30] Evidence for the secondary electron accumulation in the beam shadow is visualized in the low magnification TEM image in Fig. 2d, in which the previously irradiated area at high magnification (highlighted with yellow arrows) is surrounded by a dark rim of charge-induced volatiles accumulation. Ejection and accumulation of secondary electrons from poorly conductive specimens are known

as the Berriman effect and are,[31–33] in our case, primarily driven by the poorly conductive hydrocarbon residues and amorphous carbon layers on the graphene surface. This effect leads to the net formation of an oxidative area, caused by the fast primary electrons from the beam, and a reductive site, induced by slow secondary electrons from the specimen, which is approximately 50 nm larger in diameter than the initial irradiated area.[34] Thus, the induced electric field is dependent on the conductivity of the specimen and the electron flux, as described in Fig. 2d iii-iv.[35]

A reductive demetallation mechanism is further supported by density functional theory (DFT) calculations, in which we determined the relative threshold dissociation energy $\backslash E_d$ for the Pb release from the macrocycle. As shown in Fig. 2e, reducing **1Pb^{0}** to **1Pb^{-1}** or **1Pb^{-2}** lowers $\backslash E_d$(N_4-Pb) up to 1.7 eV, whereas an oxidative electron removal shows only marginal effects on the binding energy. Thus, the reductive demetallation is likely to proceed in the beam shadow without being witnessed by the direct microscopic observation, whereas a knock-on induced carbon displacement and thus the decomposition of macrocycle **1** is expected to proceed after a total electron dose (TED) of around 45 x 10^6 e^-nm^{-2} and therefore renders this pathway to be unlikely (compare Extended Data Table 1). Identical observations were made for strongly complexed metal derivatives **1Pt**, **1Pd**, and **1Ni** (compare Extended Data Fig. 2), which describes this phenomenon as applicable beyond weakly bound Pb-porphyrins.

Fig. 2 Electron microscopic analysis of the overall environment of the starting FP intermediate and mechanistic insights. a, Overview of starting scene. The yellow dashed circle highlights the structure of interest; the magenta-highlighted area resembles an amorphous Pb-atom aggregate; the green area the GML; the blue area an amorphous carbon layer. The colors of the FFT diffraction pattern match the selected areas. **b**, HAADF-STEM image and EDS analysis of Pb-atom aggregates: i) low-mag. HAADF-STEM, ii) high-mag. HAADF-STEM, iii) EDS elemental mapping of Pb from ii), iv) EDS spectrum. **c**, TEM simulations of pristine **1Pb** and **1** on graphene. **d**, Proposed mechanism: 1) hot electron uptake; 2) reduction of metalloporphyrin; 3) decomplexation and release of metal atom onto the substrate. **e**, i) Berriman effect-induced accumulation of charged volatiles in the periphery of the primary beam-irradiated area, ii) beam-induced electrochemical areas on the substrate, iii) beam-induced currents on the substrate, iv) charge conservation equation; I_0: Primary electron beam current, I_T: transmitted electron beam current, E: electric field vector, I_e: secondary electron current, I_+: cation flux, I_S: electron back current. **f**, Morse potential for the N_4–Pb bond elongation and determination of the bond threshold dissociation energy E_d at different charging states of **1Pb**; calculated at the density functional B3LYP/6-31G(d)/LANL2DZ>Kr level of theory.

SMART-EM analysis. With the localized structure of interest from Fig. 2a, we will now focus on the structure determination and its dynamics during the course of observation (Supplementary Video 1). At this point, the time is arbitrarily set to 0 s, as the area might have been irradiated for 3-5 s during the search for the structure prior to the recording. Thus, the received energy from the e-beam transformed **1Pb** already into a cylindrical bowl structure, as reconstructed from the atomic number (Z)-adjusted model and TEM image simulations in Fig. 3a.[36] From statistical measurements of that singular entity over all frames (t = 0 s – 7.0 s) whose circular shape persisted, the structure measured 0.89 ± 0.02 nm x 0.90 ± 0.03 nm. These dimensions, shape, and phase contrast are well reproduced by a $C_{100}H_6N_4$ model **(hemi-1')Pb** (for comparison: **1** = $C_{100}H_{54}N_4$), with 20 zipped-up C–C bonds, six remaining hydrogen atoms, and a Pb atom coordinated by carbon atoms at the lower rim. The remaining dangling carbon atoms are bound to the GML, which immobilizes the structure on the surface. During a short transition period (t = 7.5 – 9.0 s), the shape of **(hemi-1")Pb** morphs to a pentagon-shaped structure with a diameter of 0.87 ± 0.02 nm, which lasts for 2.0 s (Fig. 3b). The transition is accompanied by the loss of four hydrogen atoms, as identified by the model. The simulation with a diameter of 0.89 nm fits well within the experimental error of ± 0.02 nm.

In the period from 12.0 s to 20.5 s, several dynamic processes with severe impact on the structure take place. As displayed in Fig. 3c, a second Pb-atom, fueled from the neighboring Pb-cluster, attaches to the structure to give a **(hemi-1'")Pb_2** structure that appears to be tipped over onto the sidewall. The model suggests that an additional C–C bond has formed at this point. From there on (Fig. 3d), the structure undergoes a rolling translation of around 0.65 nm on the surface, which leads to the C–C bond formation of the last three remaining open *fjord* regions and the subsequent incorporation of both Pb atoms; one into the endohedral cavity and the second by complexation at the porphyrinic site of the skeleton.

This exotic bimetallic cage structure, denoted as **Pb@(FP-Pb)** (Fig. 3e), could be identified by an excellent match between the experimental TEM image (diameter: 0.79 ± 0.01 nm) and the

simulation (0.79 nm). Furthermore, from comparative simulations, we could verify that the metal atom is not located outside the cage (compare Extended Data Fig. 3) and thus get detailed insights about rather rare molecular Pb–Pb interactions as found in the complex. As shown in the side-view of the model, the experimentally measured Pb-Pb distance of 3.0 Å fits a model that contains a Pb–Pb single bond of 3.01 Å. While not many reports on bimetallic Pb-complexes are available,

our results fit well with the averaged Pb–Pb distance of 2.94 Å, as determined by single-crystal X-ray diffraction of molecular organo-Pb complexes.[37] All attempts simulating the structure with different Pb–Pb bond orders and at different tilting angles of the whole structure did not resolve the experimental findings (compare Extended Data Fig. 4). With these findings, we conclude **Pb@(FP-Pb)** to be remarkable in three ways: 1) It is proof of the possibility of incorporating the functional porphyrin macrocycle into a fullerene-like carbon cage. 2) It is a bimetallic species that contains a metal atom in the endohedral cavity and another as part of the skeletal structure. Previously, metalated fullerenes were limited to either endohedral or exohedral complexes only.[38,39] 3) It shows that Pb atoms, which have never been found in metallofullerenes before, can be incorporated into fullerene-like nanocages. Thus, in principle, other metal nanocages can be envisioned to be synthesized from similar bottom-up methodologies as well, which are unavailable at the moment *via* the standard arc-discharge techniques to endohedral metallofullernenes.[38]

In the last period of the movie (t = 31.5 – 43.5 s) in Fig. 3f, after a rotation of the structure, the skeletal Pb atom is ejected to leave a monometallic endohedral fullerophyrin **Pb@(FP)** behind, which remains stable under the imaging conditions for 12 s until the end of the movie. Again, this observation is significant as it proves the skeletal structure from another perspective and simultaneously highlights the envisioned reversibility of metallic complexation by the skeletal porphyrin. Furthermore, it qualitatively depicts the weakened Pb–Pb bond strength, which is indicated by the slightly increased bond length by 0.1 Å due to a reduced pyramidal inward coordination of the skeletal Pb atom. A vertically aligned structure of **Pb@(FP-Pb)**, in which the Pb atoms are placed atop of each other is unlikely, as evinced from a cross-correlation analysis of **Pb@(FP)** with **Pb@(FP-Pb)**, in which the cage structure shows poor overlap (Fig. 3g).

Fig. 3. SMART-EM Analysis of the FP formation. a, state of **(hemi-1')Pb** during the first 7 s; structure appears to have 20 closed C–C bonds and 6 remaining H atoms; dangling C atoms are bound to the surface. **b**, intermediate **(hemi-1")Pb** with morphed shape; 20 closed C–C bonds and 2 remaining H atoms. **c**, transition from a stationary structure to a pitched structure with an additional Pb atom **(hemi-1'")Pb_2**. **d**, apparent rolling of the structure over the surface. **e**, structural analysis of **Pb@(FP-Pb)**; all 24 C–C bonds closed, no remaining H atoms. **f**, Structural analysis of **Pb@(FP)**. **g**, Cross-correlation image of a simulated **Pb@(FP-Pb)** (red/blue) with vertically alligned Pb atoms and observed **Pb@(FP)** (black/white). Scale bar 1 nm.

Deconvolution of SMART-EM results. All chemical transformations are collected in a time-dependent event graph to assemble all factors and observations into a bigger picture (Fig. 4a). As depicted, the electron dose rate (EDR) of around 1.5 x 10^6 e^- nm^2s^{-1} remains nearly constant over the whole period, which leads to a linear accumulation of the TED over time. However, the observed molecular events show no linear correlation between the TED and EDR and thus appear stochastically. Nonetheless, each process, such as an H atom loss or C–C bond formation, can be correlated to a translational event of the structure on the surface.[20] A mere knock-on induced C–C bond formation *via* hydrogen atom shedding to C$^\bullet$ radicals, followed by radical recombination, can be ruled out for three reasons: 1) A significant energy contribution to the formation of the first hemi-fullerophyrin **(hemi-1')Pb** must have come already from secondary electrons in the beam shadow while scanning the area. The secondary electron flux derived from the carbon substrate at our experimental conditions is estimated to be 5.7 x 10^3 e^- $nm^{-2}s^{-1}$. However, they cannot transfer enough momentum for a homolytic C–H bond cleavage due to their reduced kinetic energy (typically <<50 eV). As shown in Fig. 4b, a minimum kinetic energy of 3500 eV is required for a knock-on induced C–H bond cleavage in **1Pb**, yet even fast secondary electrons from an inner shell oxidation of the specimen do not reach the required energy (carbon K-shell (1s) = 284 eV).[28] Nonetheless, their kinetic energy can be sufficiently low for electron attachment-induced processes, such as the hot electron reduction (*vide supra*) or a reductive cyclodehydrogenation.[40–42] 2) The knock-on displacement cross-section α_d, derived from the McKinley-Feshbach equation,[13] indicates that the earliest event of H atom shedding under direct 80 keV e-beam irradiation should occur for **1Pb** after 19 x 10^6 e^- nm^{-2}. However, even if a maximum additional irradiation time of 5 s in the pre-recording period is considered, the loss of >80% of the H atoms in **1Pb** cannot be explained. This finding indicates that the processes observed in this video are a result of a less energy-demanding chemical reaction mechanism rather than a physical fragmentation of the molecule *via* knock-on displacement.[20] This includes the demetallation of **1Pb** *via* secondary knock-on effects from fast H-atoms, which cannot overcome the threshold displacement energy of complexed Pb of around 6 eV with a maximum transferred kinetic energy of $E_{T'}$ = 3.60 eV (compare Extended Data Fig. 5). 3) The significantly larger ionization cross-section of the highest occupied molecular orbital (HOMO) α_{rBEB} by a factor of 10^5, derived from the relativistic Binary-Encounter-Bethe model,[43] suggests that the observed transformations such as the demetallation and cyclodehydrogenation reactions are redox-based processes and thus, can

be regarded as electron beam-induced electrochemical analogs to the respective wet-chemical reactions.

Another observation that can be reasoned with quantum chemical rationale is the fixation of the molecule to the graphene surface at the most-curved outer sidewall. A van der Waals-based immobilization of the molecule would prefer interactions with a larger surface area, subsequently leading to different TEM images (compare Extended Data Fig. 6). However, analogously to the reactivity of strained double bonds in fullerenes,[44,45] the ν-bond polarization resulting from the skeletal curvature facilitates the bonding to the GML *via* cycloaddition reactions. This is visualized with the electrostatic potential (ESP) map of **Pb@(FP-Pb)** (Fig. 4c), which shows the strongest polarization compared to **FP** or **Pb@(FP)** (compare Extended Data Fig. 7a). In view of the frontier molecular orbitals and therefore the cycloaddition chemistry of fullerophyrins, metalation of **FP** lifts the energy level of the highest occupied molecular level (HOMO), which is located at the outer curvature of the cage, while the lowest unoccupied molecular orbital (LUMO) remains nearly unaffected (Fig. 4d). Ionization on the other hand, is dominated by the soft metal atoms of **Pb@(FP)** and **Pb@(FP-Pb)** (Fig 4e, and Extended Data Fig. 7b).

Fig. 4. Summary of events and electronic characteristics of fullerophyrins. a, Number of events, total electron dose (TED), and electron dose rate (EDR), plotted against the time. **b**, Theoretical ionization cross-section (α_{rBEB}) of **1**(HOMO) and knock-on displacement cross-section (α_d) for H, C, and N atoms calculated for **1**. **c**, Electrostatic potential map of **Pb@(FP-Pb)** (color range from -30 to +20 kJ/mol, isovalue 0.002 e/au^3). **d**, Energy distribution of frontier molecular orbitals of **FP**, **Pb@(FP)**, and **Pb@(FP-Pb)** (isovalue 0.032 √(e/au^3)). **e**, Sliced contour plot of the ionization potential of **FP**, **Pb@(FP)**, and **Pb@(FP-Pb)** (color range from 8 to 15 eV). DFT level: B3LYP-D3/6-31G(d)/LANL2DZ>Kr.

Conclusion

Although first studies of matter under the influence of radiation can be dated back to the 19th century,[46] the understanding of fast electron-induced molecular reactions is still in its infancy. Enabled through the radiation chemical cyclodehydrogenation, we demonstrated the transformation of a benzoporphyrin precursor **1Pb** to a designer-made doubly-holed fullerene-porphyrin cage structure **FP** by in-depth SMART-EM analysis. Simultaneously, we evidenced the ability of **FP** to host up to two Pb atoms, which led to the exotic formation of bimetallic **Pb@(FP-Pb)** and the monometallic endohedral **Pb@(FP)**. Subsequent insights about the complexation dynamics and the Pb–Pb binding motif of this organometallic cage structure were obtained. From the observations, we conclude that not only the fast primary electrons have to be considered for chemical transformations, but also the much slower secondary electrons in the beam shadow. The latter electron species might be responsible for the demetalation of the porphyrins *via* a hot-electron reduction, as well as the partial C–C bond formation to **(hemi-1')Pb** *via* a reductive cyclodehydrogenation. In contrast, the final cyclodehydrogenation reaction to the strained fullerene-like cage structure occurs under an oxidative primary 80 kV beam. With these cinematographic insights, we believe that SMART-EM will serve not only as an analytical tool for physical organic chemists but will resolve the synthetic capacity that can be expected from focused electron beam-induced reactions. Consequently, understanding radiation chemistry on the molecular level will tremendously impact the design and fabrication of well-defined topological nanostructures by e-beam lithographic techniques.[35,47]

Online Content

The authors declare that the data supporting the findings of this study are available within the paper and its supplementary information files.

Supporting Information. The following files are available free of charge. PDF file (Captions for Video S1 to S3, Supplementary Synthetic Details, Supplementary Description of Cross-Section Calculation, Supplementary Computational Details, XYZ Coordinates, NMR and MS Spectral Appendix, Supplementary Text, Figures S1 to S36, Supplementary Tables S1 to S19, Supplementary References), and AVI video files (Video S1 to S3).

Methods

General synthetic methods. Chemicals were purchased from Sigma-Aldrich and used without further purification. Solvents were distilled prior to usage. CH_2Cl_2 was neutralized with K_2CO_3 prior to distillation. Et_2O was dried over CaH_2 and distilled prior to usage. Reactions were carried out under a dry N_2 or Ar atmosphere, using standard Schlenk techniques. Further synthetic details are described in the Supplementary Information.[48]

Synthesis of 1. Pyrene-2-carbaldehyde **3** (0.489 g; 2.12 mmol) and 4,7-dihydro-2*H*-ethanoisoindole **2** (0.307 g; 2.11 mmol) were dissolved in CH_2Cl_2 (125 mL) in a 250 mL Schlenk flask under N_2. The solution was purged with N_2 for 15 min before $BF_3{\cdot}OEt_2$ (0.075 mL, 0.61 mmol) was added. The mixture was stirred for 20 h at rt under light exclusion. Then DDQ (0.475 g; 2.09 mmol) was added, and the mixture was brought to reflux for 2 h under N_2. After cooling to rt, the mixture was washed with a solution of 10% aqueous Na_2SO_3 (125 mL) and 10% Na_2CO_3 (125 mL). The phases were separated, and the solvent was removed under vacuum. Then the crude product was heated under vacuum to 200 °C for 1.5 h. After cooling to rt, the solid was dissolved in CH_2Cl_2 and purified by plug filtration (SiO_2, diameter 4 cm; height: 8 cm; CH_2Cl_2 + 1% TFA). The final purification was carried out by recrystallization (MeOH/CH_2Cl_2). The product was isolated as a dark green solid in 81% yield (0.565 g; 0.431 mmol).[49–51]

Synthesis of 1Pb. In a flame-dried Schlenk tube, $Pb(OAc)_2x3H_2O$ (22 mg; 57 µmol, 15 equiv) was dissolved in DMF (1.0 mL) under N_2 and heated to 135 °C for 5 min. 5,10,15,20-tetrakis(2-pyrenyl)tetrabenzoporphyrin **1** (5.0 mg; 3.8 µmol) was added, and the mixture was heated to 140 °C for 2 h. The reaction was cooled to rt, and the solvent was removed in vacuum. The crude product was re-dissolved in a small amount of CH_2Cl_2 and precipitated with MeOH. The precipitate was filtered and washed several times with MeOH. The brownish, slightly purple product (around 4 mg) was collected and stored in the vacuum on a hydrophobic PTFE filter paper until used for TEM experiments.

Synthesis of 2. 4,7-dihydro-2*H*-ethanoisoindole **2** was prepared according to a procedure by Ruppel *et al*. Spectral data agreed with respective literature data.[49]

Synthesis of 3. 2-Bromopyrene **4** (1.0 g, 3.56 mmol) was suspended in Et_2O (50 mL) under N_2 in a 250 mL Schlenk flask and cooled to -20 °C (ice water/salt mixture). *n*-BuLi 1.6 M in hexanes (5.0 mL, 8.0 mmol, 2.2 equiv) was added slowly under N_2, and the reaction mixture was stirred for 1h at -20 °C. Then the bath was removed, and the mixture was stirred for another 30 min at rt. After the addition of DMF (10 mL, 144 mmol, 40 equiv), the mixture was stirred for 1 h at rt. The reaction was quenched carefully with 10% HCl solution, and the organic layer was evaporated. The mixture was extracted with CH_2Cl_2 (2x150 mL), and the combined organic layers were washed with water (2x150 mL) and brine (150 mL) before they were dried over $MgSO_4$ and filtered. The solvent was removed by rotary evaporation. The crude product was adsorbed on silica gel and purified *via* column chromatography (SiO_2, diameter: 5 cm, height: 30 cm, CH_2Cl_2:hexanes = 3:2). The product was isolated as a pale-yellow solid in 53% yield (0.43 g, 1.87 mmol).

Synthesis of 4. 2-bromopyrene **4** was synthesized according to a procedure by Crawford *et al*. Spectral data agreed with respective literature data.[52]

TEM grid preparation. CVD-grown monolayer graphene-coated quantifoil gold-grids, with a hole size of 2 µm and space between the holes of 4 µm, were purchased from Graphenea. Prior to usage, the graphene grids were purified with activated carbon using a modified dry-cleaning protocol.[20,53] A small amount of dried activated carbon was placed into a petri dish, and the graphene grid was carefully placed atop and then fully covered with another portion of activated carbon. The petri dish was placed in a furnace under ambient conditions and annealed: 1) rt to 210 °C in 45 min (heating rate around 4.6°C/min); 2) 210 °C for 30 min; 3) cooling to 120 °C in 30 min. The grid was stored at 120 °C under activated carbon until it was used for the sample preparation. The grid was then mechanically cleaned from the activated carbon, using a gentle stream of dry N_2 for several minutes.

Sample preparation. A 10^{-5} M solution of **1Pb** (10 µL) in THF was freshly prepared by dissolving the solid from the PTFE filter paper in THF (3 mL) before drop-casting one drop onto the dry-cleaned graphene grid. The excess sample solution was removed with a filter paper. The sample grid was cleaned with two cycles of MeOH (10 µL), followed by the removal of excess solvent with a filter paper. The grid was then pre-dried in high vacuum at 5 ξ 10^{-5} Pa for 2 h before introducing the sample into the TEM chamber.

SMART-EM, STEM, and EDS elemental mapping. Observations were carried out on a cold FEG JEOL JEM-ARM200F instrument, equipped with a Cs aberration corrector and JED-2300T Energy Dispersive X-ray Spectrometer, at an acceleration voltage of 80 kV and a vacuum of 1 ξ 10^{-5} Pa in the specimen chamber. Experiments were carried out on a heating holder (JEOL EM-21130). To remove volatile impurities from the specimen, the holder was heated at 573 K for 30–60 min without electron irradiation before cooling to 298 ± 5 K. After the stage temperature settled to the target value, we waited for an additional 30 min to minimize thermal drift. EM videos were recorded on a CMOS camera (Gatan OneView, 4,096 ξ 4,096 pixels) operated in binning 2 mode (output image size: 2,048 ξ 2,048 pixels, pixel resolution 0.021 nm at ξ1000,000), with an exposure time of 500 ms and a framerate of 2 fps. All images were automatically processed on Gatan DigitalMicrograph software. The specimen was screened for viable candidates at low dose conditions (≈10^{-5} $e^{-}s^{-1}nm^{-2}$) to suppress e-beam-induced processes as much as possible. The typical time between finding and starting the recording of a respective scene was 1 to 3 s. STEM and EDS elemental mapping were carried out on a beryllium holder (JEOL EM-21130) at room temperature. HAADF STEM detector was used with a camera length of 8 cm (with detection angles ranging from 68 to 280mrad). The Probe size was 7C (60 pA), and the CL aperture size was 40 µm. The probe convergence angle was X (something between 28 to 33mrad).

Image processing. Images were collected in the .dm3 format on Gatan DigitalMicrograph software and processed using ImageJ 1.51f software.[54] To remove the unevenness of the electron irradiation, all images were processed by a bandpass filter (filtering structures smaller than 3 pixels and larger than 40 pixels, tolerance of direction: 5%), and contrast/brightness adjusted. Prior to analysis, images were subjected to a thermal drift correction. TEM simulation images were corrected according to the TEM experiment's electron dose rate and generated using a multi-slice procedure implemented in the Bionet elbis software.[55] Simulation parameters were set to agree with the actual experimental parameters: acc. Volt. = 80.00 kV, ′A = 0.04176 Å, Cs = -0.003 mm, df = 120 Å, Cc = 1.25 mm, de = 0.60 eV, α = 0.20 mrad, OL Aperture radius = 20.88 mrad, OL Aperture radius = 0.50 $Å^{-1}$, pixel size = 0.0210844, max. Intens. = 1.1278. The simulations were processed analogously to the experimental TEM images to obtain the best correlation.

Single-molecule statistical analysis. Single-molecule statistics were carried out from the plot profile analysis of the observed intermediate structures. The black maxima in the profile were used and measured as a reference point. The standard deviation was calculated according to Eq. 1.

$$\sigma = \sqrt{\frac{\sum_{i=1}^{n}(x_i - \bar{x})^2}{n-1}} \qquad \text{Eq. 1}$$

DFT calculations. Geometry optimization and energy calculations were performed on Q-Chem as implemented in the SPARTAN '20 work package.[56,57] Structures were optimized using the Head Gordon range-separated global hybrid generalized gradient approximation functional ωB97X-D with Grimme D2 dispersion correction.[58] Geometry optimization and initial evaluation of the molecules' energies were performed with the Pople-type dual basis split-valence triple-ζ/double-ζ quality basis set 6-311G(d,p)[6-31G(d)]. Thermochemical calculations were obtained using the Minnesota global hybrid meta generalized gradient approximation functional M06-2X with 54% Hartree-Fock exchange[59] in combination with the Ahlrichs-Weigend triple-ζ quality basis set def2-TZVP.[60] Further computational details and the calculations of cross-sections using the McKinley Feshbach approximation and the relativistic Binary encounter Bethe model are described in the Supplementary Information.

Acknowledgement

The research was supported by the Institute for Basic Science (IBS-R026-Y1, IBS-R026-D1), JSPS (KAKENHI JP19H05459), Japan Science and Technology Agency (CREST JPMJCR20B2), and the Deutsche Forschungsgemeinschaft (DFG, Projektnummer 182849149, SFB 953). H.H. and D.L. acknowledge the support as an International Research Fellow from the Japan Society for the Promotion of Science (JSPS). H.H. further thanks the Bavarian Equal Opportunities Sponsorship − Realisierung von Chancengleichheit von Frauen in Forschung und Lehre (FFL) − Realization Equal Opportunities for Women in Research and Teaching, for financial support. D.L. further thanks the Alexander von Humboldt Foundation (AvH) for a Feodor-Lynen return fellowship.

Author Contributions

D.L. conceptualized the project and wrote the manuscript with feedback from all authors. All authors discussed the results and commented on the manuscript. N.J. and K.Y.A. designed the molecule. H.H. synthesized and characterized the molecules. H.H. and D.L. carried out the TEM experiments. S.L. carried out the STEM/EDS experiments and analysis. D.L. carried out SMART-EM data analysis, DFT calculations, and EM simulations. K.H. and E.N. provided access and maintenance of the TEM. E.N., N.J., and D.L. were responsible for funding acquisition. All authors approved the final version of the manuscript.

Competing Interests statement

The authors declare no competing interests.

References

1. Nakamura, E. Atomic-Resolution Transmission Electron Microscopic Movies for Study of Organic Molecules, Assemblies, and Reactions: The First 10 Years of Development. *Acc. Chem. Res.* **50**, 1281–1292 (2017).

2. Skowron, S. T. *et al.* Chemical Reactions of Molecules Promoted and Simultaneously Imaged by the Electron Beam in Transmission Electron Microscopy. *Acc. Chem. Res.* **50**, 1797–1807 (2017).

3. Nakamuro, T., Sakakibara, M., Nada, H., Harano, K. & Nakamura, E. Capturing the Moment of Emergence of Crystal Nucleus from Disorder. *J. Am. Chem. Soc.* **143**, 1763–1767 (2021).

4. Xing, J., Schweighauser, L., Okada, S., Harano, K. & Nakamura, E. Atomistic structures and dynamics of prenucleation clusters in MOF-2 and MOF-5 syntheses. *Nat. Commun.* **10**, 3608 (2019).

5. Nakamuro, T. *et al.* Time-Resolved Atomistic Imaging and Statistical Analysis of Daptomycin Oligomers with and without Calcium Ions. *J. Am. Chem. Soc.* **144**, 13612–13622 (2022).

6. Biskupek, J. *et al.* Bond Dissociation and Reactivity of HF and H2O in a Nano Test Tube. *ACS Nano* **14**, 11178–11189 (2020).

7. Cao, K. *et al.* Imaging an unsupported metal–metal bond in dirhenium molecules at the atomic scale. *Sci. Adv.* **6**, eaay5849 (2020).

8. Jordan, J. W. *et al.* Single-molecule imaging and kinetic analysis of intermolecular polyoxometalate reactions†. *Chem. Sci.* **12**, 7377–7387 (2021).

9. Cao, K. *et al.* Atomic mechanism of metal crystal nucleus formation in a single-walled carbon nanotube. *Nat. Chem.* **12**, 921–928 (2020).

10. Kharel, P. *et al.* Atomic-Resolution Imaging of Small Organic Molecules on Graphene. *Nano Lett.* **22**, 3628–3635 (2022).

11. Mirzayev, R. *et al.* Buckyball sandwiches. *Sci. Adv.* **3**, e1700176 (2017).

12. Choe, J. *et al.* Direct imaging of structural disordering and heterogeneous dynamics of fullerene molecular liquid. *Nat. Commun.* **10**, 4395 (2019).

13. Susi, T., Meyer, J. C. & Kotakoski, J. Quantifying transmission electron microscopy irradiation effects using two-dimensional materials. *Nat. Rev. Phys.* **1**, 397–405 (2019).

14. Cai, Z., Chen, S. & Wang, L.-W. Dissociation path competition of radiolysis ionization-induced molecule damage under electron beam illumination. *Chem. Sci.* **10**, 10706–10715 (2019).

15. Egerton, R. F. Radiation damage to organic and inorganic specimens in the TEM. *Micron* **119**, 72–87 (2019).

16. Liu, D. *et al.* Ionization and electron excitation of C_{60} in a carbon nanotube: A variable temperature/voltage transmission electron microscopic study. *Proc. Natl. Acad. Sci.* **119**, e2200290119 (2022).

17. Chamberlain, T. W. *et al.* Isotope Substitution Extends the Lifetime of Organic Molecules in Transmission Electron Microscopy. *Small* **11**, 622–629 (2015).

18. Okada, S. *et al.* Direct Microscopic Analysis of Individual C60 Dimerization Events: Kinetics and Mechanisms. *J. Am. Chem. Soc.* **139**, 18281–18287 (2017).

19. Shimizu, T., Lungerich, D., Harano, K. & Nakamura, E. Time-Resolved Imaging of Stochastic Cascade Reactions over a Submillisecond to Second Time Range at the Angstrom Level. *J. Am. Chem. Soc.* **144**, 9797–9805 (2022).

20. Lungerich, D. *et al.* A Singular Molecule-to-Molecule Transformation on Video: The Bottom-Up Synthesis of Fullerene C_{60} from Truxene Derivative C60H30. *ACS Nano* **15**, 12804–12814 (2021).

21. Scott, L. T. *et al.* A rational chemical synthesis of C_{60}. *Science* **295**, 1500–1503 (2002).

22. Boorum, M. M., Vasil'ev, Y. V., Drewello, T. & Scott, L. T. Groundwork for a rational synthesis of C60: cyclodehydrogenation of a $C_{60}H_{30}$ polyarene. *Science* **294**, 828–831 (2001).

23. Chuvilin, A., Kaiser, U., Bichoutskaia, E., Besley, N. A. & Khlobystov, A. N. Direct transformation of graphene to fullerene. *Nat. Chem.* **2**, 450–453 (2010).

24. Cao, K. *et al.* Comparison of atomic scale dynamics for the middle and late transition metal nanocatalysts. *Nat. Commun.* **9**, 3382 (2018).

25. Lungerich, D. *et al.* Gas-Phase Transformation of Fluorinated Benzoporphyrins to Porphyrin-Embedded Conical Nanocarbons. *Chem. Eur. J.* **26**, 12180–12187 (2020).

26. Xie, W. & Schlücker, S. Hot electron-induced reduction of small molecules on photorecycling metal surfaces. *Nat. Commun.* **6**, 7570 (2015).

27. Kim, M., Lin, M., Son, J., Xu, H. & Nam, J. Hot-Electron-Mediated Photochemical Reactions: Principles, Recent Advances, and Challenges. *Adv. Opt. Mater.* **5**, 1700004 (2017).

28. Brydson, R. *Electron Energy Loss Spectroscopy*. (Taylor & Francis, 2001). doi:10.1201/9781003076858-1.

29. Kumar, M., Neta, P., Sutter, T. P. G. & Hambright, P. One-electron reduction and demetallation of copper porphyrins. *J. Phys. Chem.* **96**, 9571–9575 (1992).

30. Cowan, J. A. & Sanders, J. K. M. Reductive demetallation of porphyrins: Evidence for peripheral and axial modes of reduction. *Tetrahedron Lett.* **27**, 1201–1204 (1986).

31. Russo, C. J. & Henderson, R. Charge accumulation in electron cryomicroscopy. *Ultramicroscopy* **187**, 43–49 (2018).

32. Downing, K. H., McCartney, M. R. & Glaeser, R. M. Experimental Characterization and Mitigation of Specimen Charging on Thin Films with One Conducting Layer. *Microsc. Microanal.* **10**, 783–789 (2004).

33. Brink, J., Sherman, M. B., Berriman, J. & Chiu, W. Evaluation of charging on macromolecules in electron cryomicroscopy. *Ultramicroscopy* **72**, 41–52 (1998).

34. Kuei, B. & Gomez, E. D. Pushing the limits of high-resolution polymer microscopy using antioxidants. *Nat. Commun.* **12**, 153 (2021).

35. Gonzalez-Martinez, I. G. *et al.* Electron-beam induced synthesis of nanostructures: a review. *Nanoscale* **8**, 11340–11362 (2016).

36. Xing, J. *et al.* Atomic-number (Z)-correlated atomic sizes for deciphering electron microscopic molecular images. *Proc. Natl. Acad. Sci.* **119**, e2114432119 (2022).

37. Wang, Y., Quillian, B., Wei, P., Yang, X.-J. & Robinson, G. H. New Pb–Pb bonds: syntheses and molecular structures of hexabiphenyldiplumbane and tri(trisbiphenylplumbyl)plumbate. *Chem. Commun.* **0**, 2224–2225 (2004).

38. Popov, A. A., Yang, S. & Dunsch, L. Endohedral Fullerenes. *Chem. Rev.* **113**, 5989–6113 (2013).

39. Nakamura, E. Bucky ferrocene and ruthenocene: serendipity and discoveries. *J. Organomet. Chem.* **689**, 4630–4635 (2004).

40. Kawahara, K. P., Matsuoka, W., Ito, H. & Itami, K. Synthesis of Nitrogen-Containing Polyaromatics by Aza-Annulative π-Extension of Unfunctionalized Aromatics. *Angew. Chem. Int. Ed.* **59**, 6383–6388 (2020).

41. Wang, C., Sun, Q., García, F., Wang, C. & Yoshikai, N. Robust Cobalt Catalyst for Nitrile/Alkyne [2+2+2] Cycloaddition: Synthesis of Polyarylpyridines and Their Mechanochemical Cyclodehydrogenation to Nitrogen-Containing Polyaromatics. *Angew. Chem. Int. Ed.* **60**, 9627–9634 (2021).

42. Rickhaus, M., Belanger, A. P., Wegner, H. A. & Scott, L. T. An Oxidation Induced by Potassium Metal. Studies on the Anionic Cyclodehydrogenation of 1,1′-Binaphthyl to Perylene. *J. Org. Chem.* **75**, 7358–7364 (2010).

43. Kim, Y.-K., Santos, J. P. & Parente, F. Extension of the binary-encounter-dipole model to relativistic incident electrons. *Phys. Rev. A* **62**, 052710 (2000).

44. Stevenson, S. *et al.* Semiconducting and Metallic [5,5] Fullertube Nanowires: Characterization of Pristine D5h(1)-C90 and D5d(1)-C100. *J. Am. Chem. Soc.* **143**, 4593–4599 (2021).

45. Hirsch, A. & Brettreich, M. *Fullerenes*. (WILEY-VCH Verlag, 2005).

46. Kinchin, G. H. & Pease, R. S. The Displacement of Atoms in Solids by Radiation. *Rep. Prog. Phys.* **18**, 1 (1955).

47. Egerton, R. Radiation Damage and Nanofabrication in TEM and STEM. *Microsc. Today* **29**, 56–59 (2021).

48. Hölzel, H. *Hybrid architectures based on carbon-rich pi-systems and porphyrins*. (Friedrich-Alexander University Erlangen-Nuernberg, 2021).

49. Ruppel, M. *et al.* A Comprehensive Study on Tetraaryltetrabenzoporphyrins. *Chem. Eur. J.* **26**, 3287–3296 (2020).

50. Ruppel, M., Gazetas, L.-P., Lungerich, D., Hampel, F. & Jux, N. Investigations of Low-Symmetrical Tetraaryltetrabenzoporphyrins Produced by Mixed Condensation Reactions. *J. Org. Chem.* **85**, 7781–7792 (2020).

51. Ruppel, M., Gazetas, L.-P., Lungerich, D. & Jux, N. Synthesis and Photophysical Properties of Hexabenzocoronene-Tetrabenzoporphyrin Architectures. *Eur. J. Org. Chem.* **2020**, 6352–6360 (2020).

52. Crawford, A. G. *et al.* Synthesis of 2- and 2,7-Functionalized Pyrene Derivatives: An Application of Selective C–H Borylation. *Chem. Eur. J.* **18**, 5022–5035 (2012).

53. Algara-Siller, G., Lehtinen, O., Turchanin, A. & Kaiser, U. Dry-cleaning of graphene. *Appl. Phys. Lett.* **104**, 153115 (2014).

54. Schneider, C. A., Rasband, W. S. & Eliceiri, K. W. NIH Image to ImageJ: 25 years of image analysis. *Nature methods* **9**, 671–675 (2012).

55. Hosokawa, F., Shinkawa, T., Arai, Y. & Sannomiya, T. Benchmark test of accelerated multi-slice simulation by GPGPU. *Ultramicroscopy* **158**, 56–64 (2015).

56. Shao, Y. *et al.* Advances in molecular quantum chemistry contained in the Q-Chem 4 program package. *Molecular Physics* **113**, 184–215 (2015).

57. Shao, Y. *et al.* Advances in methods and algorithms in a modern quantum chemistry program package. *Physical Chemistry Chemical Physics* **8**, 3172–3191 (2006).

58. Chai, J.-D. & Head-Gordon, M. Long-range corrected hybrid density functionals with damped atom-atom dispersion corrections. *Physical Chemistry Chemical Physics* **10**, 6615–6620 (2008).

59. Zhao, Y. & Truhlar, D. G. The M06 suite of density functionals for main group thermochemistry, thermochemical kinetics, noncovalent interactions, excited states, and transition elements: Two new functionals and systematic testing of four M06-class functionals and 12 other functionals. *Theoretical Chemistry Accounts* **120**, 215–241 (2008).

60. Weigend, F. & Ahlrichs, R. Balanced basis sets of split valence, triple zeta valence and quadruple zeta valence quality for H to Rn: Design and assessment of accuracy. *Physical Chemistry Chemical Physics* **7**, 3297–3305 (2005).

Cyclodehydrogenation steps

Extended Data Fig. 1. Thermochemical comparison of the cyclodehydrogenation reaction of $C_{60}H_{30}$ to C_{60} and 1 to FP. a, Reaction equation for the $C_{60}H_{30}$ to C_{60} conversion. **b**, Relative energies of intermediates for each reaction. **c**, Energy difference between each reaction intermediate. (DFT: M06-2X/def2-TZVP).

Extended Data Fig. 2. Characterization of 1M (M = Pt, Pd, Ni) species. a, UV/Vis analysis in THF at rt. Spectra are normalized at the absorption maximum of pyrene at 341 nm. **b**, TEM image of Pt, Pd, and Ni-atom aggregates. **c**, Low-mag TEM image of single metal atoms from **1M** species. **d**, Time-dependent diffusion of single Pt-atoms. **e**, Time-dependent diffusion of single Pt-atoms. Arrows indicate the direction of motion.

Extended Data Fig. 3. Alternative simulations with an outside bound Pb atom instead of an endohedral metal atom. The surface of the molecule displays the van der Waals surface. In the side view, the graphene is depicted as a CPK model. Scale bar 1 nm.

Extended Data Fig. 4. Simulation analysis of Pb-Pb distance in Pb@(FP-Pb) at various tilting angles. The measured angle is derived from the static graphene surface and the tilted molecule along the Pb-Pb bond. **a**, Pb-Pb single bond. **b**, non-bonded Pb atoms. Scale bar 1 nm.

Extended Data Fig. 6. Additional simulation images of Pb@(FP-Pb) with graphene's most significant van der Waals surface interactions. Scale bar 1 nm.

Extended Data Fig. 7. Electronic evaluation of different Pb-, Ge-, and Zn-fullerophyrins. a, Electrostatic potential map of **FP**, **(FP-M)**, **M@(FP)**, and **M@(FP-M)** (color range from -30 to +20 kJ/mol, isovalue 0.002 e/au^3) **b**, Sliced contour plot of the ionization potential of **FP**, **(FP-M)**, **M@(FP)**, and **M@(FP-M)** (color range from 7 to 15 eV). Black digits indicate natural atomic charge of metal atoms. DFT level: B3LYP-D3/6-311G(2d,p)//µB97X-D/6-31G(d) for Zn and Ge derivatives, B3LYP-D3/6-31G(d)/LANL2DZ>Kr for Pb-derivatives.

Extended Data Table 1. Expected knock-on-induced events of 1. Summary on the threshold displacement energies E_d, the resulting displacement cross-section α_d at 80 keV, and the minimum total electron dose TED_d for the homolytic C–H or C–C bond cleavage in **1**; calculated at the M06-2X/def2-TZVP[6-31G(d)] level of theory for C–*H*, μB97X-D/6311G(d,p) for C–*C*, and B3LYP/6-31G(d)/LanL2DZ>Kr for C-*N*-Pb.

Time-resolved imaging and analysis of the electron beam-induced formation of an open-cage metallo-azafullerene

Helen Hoelzel,[3,5] Sol Lee,[1] Konstantin Yu. Amsharov,[6] Norbert Jux,[5] Koji Harano,[3,4] Eiichi Nakamura,[3] Dominik Lungerich,[1,2,3]*

[1] Center for Nanomedicine (CNM), Institute for Basic Science (IBS), IBS Hall, 50 Yonsei-ro, Seodaemun-gu, Seoul, 03722, South Korea.

[2] Graduate Program of Nano Biomedical Engineering (NanoBME), Advanced Science Institute, Yonsei University, Seoul, 03722, South Korea.

[3] Department of Chemistry, The University of Tokyo, 7-3-1 Hongo, Bunkyo-ku, Tokyo 113-0033, Japan.

[4] Research Center for Advanced Measurement and Characterization, National Institute for Materials Science, 1-1 Namiki, Tsukuba 305-0044, Japan.

[5] Department of Chemistry and Pharmacy, Organic Chemistry II, Friedrich-Alexander-University Erlangen-Nuernberg (FAU), Nikolaus-Fiebiger-Str. 10, 91058, Erlangen, Germany.

[6] Department of Chemistry, Martin-Luther-University Halle-Wittenberg, Kurt-Mothes-Str. 2, 06120 Halle, Germany.

Email: d.lungerich@yonsei.ac.kr

Abstract: The bottom-up synthesis of strained hollow cage structures, such as fullerenes, using traditional thermal or photochemical methods remains one of the most challenging tasks in organic chemistry. Here, we demonstrate the synthetic use of an electron beam by in-depth single-molecule atomic resolution time-resolved transmission electron microscopy studies to induce the formation of an elusive doubly-holed fullerene-porphyrin cage structure from a well-defined benzoporphyrin precursor deposited on graphene. Through real-time imaging, we analyze the hybrid's peculiar ability to host up to two Pb atoms and subsequently gain insights into the dynamics of the Pb–Pb binding motif in this exotic metallo-organic cage structure. Through density functional theory calculations and image simulations, we conclude that the much slower secondary electrons, which accumulate in the irradiated area's periphery, can also initiate chemical reactions. Consequently, designing advanced carbon nanostructures by e-beam lithography will depend on the understanding and limitations of molecular radiation chemistry.

Keywords: molecular imaging; radiation chemistry; cinematic chemistry; single-molecule dynamics; DFT-modeling; transmission electron microscopy.

Technological advancements in high-resolution transmission electron microscopy (HRTEM) enabled single-molecule atomic-resolution time-resolved electron microscopy (SMART-EM)[1] or "*Chem*TEM" [2] techniques to literally change the chemists' view on molecular processes in real space and real-time analyses. A few recent highlights are the visualization and study of the NaCl nucleus emergence,[3] the prenucleation of MOF-2 and MOF-5,[4] the imaging of daptomycin molecules with and without calcium ions,[5] the bond-dissociation of HF and H_2O molecules in endohedral fullerenes,[6] the unsupported metal-metal bond in a Re_2 molecule,[7] the reactivity of metal clusters and polyoxometalates,[8,9] as well as ordered molecular superstructures.[10–12] However, the magnificent potential to observe dynamic events at the smallest scale of matter, namely at the atomic and molecular level, comes at a price and is generally described as radiation damage.[13–15] Typical destructive mechanisms include the material's ionization and subsequent destructive transformations (radiolysis) and the homolytic displacement of atoms from the structure, which received sufficient kinetic energy from the e-beam (knock-on displacement). These destructive effects are highly dependent on the specimen itself and vary with the elemental composition, binding characteristics, and electronic structure; however, also the imaging conditions, such as the acceleration voltage, the electron flux and total dose, as well as the temperature settings will impact the lifetime of molecular intermediates during SMART-EM imaging critically.[16]

On the other hand, from meticulously carried out cinematographic analyses of single-molecule reactions, several constructive and now well-understood reaction mechanisms were identified to occur under the e-beam. Apart from the homolytic dissociation of C–H bonds into radical pairs ($C^{\bullet}$ and $H^{\bullet}$) followed by subsequent radical recombination chemistry,[6,17] the [2 + 2] cycloaddition reaction of fullerenes,[16,18] and the Stone-Wales rearrangement to, for instance, peanut-shaped C_{120} nanotubes, have been identified.[19] However, compared to the continuously growing repertoire of thermally, photochemically, or mechanically initiated organic reaction mechanisms developed in wet-chemical laboratories, only a little knowledge about the control and selectivity of e-beam-induced mechanisms has been accumulated so far.[1,2] Recently, we identified another reaction mechanism proceeding under the electron beam in the pre-programmed synthesis of fullerene C_{60}, namely the cyclodehydrogenation.[20] While this particular reaction was not achieved photochemically or thermally in solution, carried out under flash vacuum pyrolysis condition at 1000 °C, the reaction outcome is regioselective.[21,22] Importantly, it is not the result of a

thermodynamically driven rearrangement of carbon atoms to fullerene C_{60}, as known from the arc-discharge synthesis of fullerenes from graphite.[23]

This study shows the *de novo* design and synthesis of a three-dimensional π-conjugated molecular nanostructure, enabled through the e-beam-induced cyclodehydrogenation reaction in the TEM. As elucidated from cinematographic SMART-EM analyses, the designed lead(II)-containing benzoporphyrin precursor **1Pb**, is shown to selectively zip up the respective *fjord* and *cove* region C–C bonds to form a three-dimensional hollow cage structure, an open-cage azafullerene, and freely diffusing Pb-atoms found on the graphene surface can be incorporated into the structure; one Pb atom as part of the endohedral cavity and another one complexed by the porphyrin macrocycle of the carbon exoskeleton. Correlated with electron-dose corrected TEM simulations and density functional theory (DFT) calculations, we identified this exotic hybrid structure and several key intermediates during its formation and subsequently gained mechanistic insights into the e-beam-induced transformations on the molecular level.

Results and discussion

Design and synthesis. We envisioned using the electron beam as a synthetic and imaging tool to induce and observe the formation of a fullerene-porphyrin hybrid **FP** ($C_{100}H_4N_4$) *via* the e-beam-induced cyclodehydrogenation reaction. For that purpose, we designed and synthesized 2-pyrenyl substituted benzoporphyrin **1** ($C_{100}H_{54}N_4$) *via* modified Lindsey condensation conditions (Fig. 1a) from masked isoindole **2** and 2-formylpyrene **3**; thermal unmasking of the isoindole moieties gave **1** in 81% overall yield. **3** was obtained in 53% yield after a lithium-halogen exchange of 2-bromopyrene **4**, followed by formylation with DMF. To introduce a high-contrast metal atom, **1** was metalated to **1Pb** ($C_{100}H_{52}N_4Pb$) using $Pb(OAc)_2$ in DMF at elevated temperature. We chose Pb as the central metal for the following reasons: 1) It has a high *Z*-contrast in TEM imaging, which facilitates the SMART-EM observations; 2) Unlike catalytically active transition metals with comparable contrast properties, such as platinum,[24] Pb as a p-block element is unlikely to undergo C-H bond activation reactions or other C–C bond-forming reactions under the electron beam. The successful metalation is easily verified by absorption spectroscopy through the significant Soret and Q-bands shifts of the metalated benzoporphyrin (Fig. 1b), whereas the absorption characteristics of the pyrene moieties remain nearly unaffected.

As predicted by DFT calculations, a consecutive zipping-up of the pyrenyl substituents with the benzoporphyrin core,[25] the resulting eight five-membered rings in the framework lead to a distortion of the initial saddle structure of **1Pb** (C_{2v} symmetry) to a C_{4v} symmetrical onion-shaped sphere with two opposing entrances to the endohedral cavity (Fig. 1c). The structure of the open-cage atoms, including the complexed metal atom, follows the isolated pentagon rule (IPR) for fullerenes. However, the IPR conditions are not met upon closing the lower rim in **FP** to twelve pentagons through the substitution of the hydrogen atoms by a quaternary fenestrane-type carbon atom (Fig. 1d). The thermochemical analysis (Fig. 1e) at the density functional M06-2X/def2-TZVP//ωB97X-D/6-31G(d) level of theory reveals an increase in relative energy over the consecutive 24 cyclodehydrogenation steps to around 30.1 eV, which corresponds to an average ΔE per step of 1.25 eV. In comparison, this value is less than for forming fullerene C_{60} from truxene derivative $C_{60}H_{30}$, which requires around 1.4 eV per step (compare Extended Data Fig. 1).[20] Thus, from a thermochemical perspective, the precursor design appears reasonable.

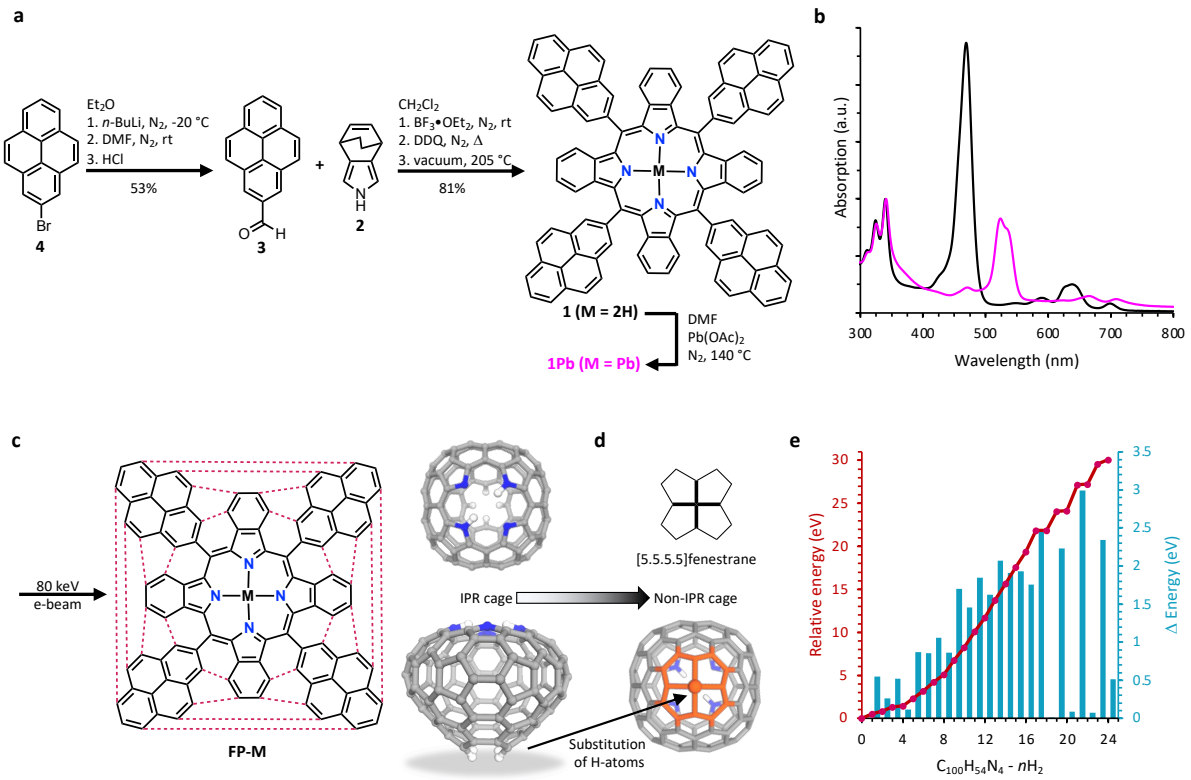

Fig. 1. Experimental and computational approach to fullerophyrin FP. **a**, Wet-chemical synthesis of benzoporphyrin precursor **1Pb**. **b**, Absorption spectra of **1** and **1Pb** in CH_2Cl_2 at rt, spectra normalized to pyrene's p-band. **c**, Electron beam-induced cyclodehydrogenation to **FP**. Top and side view of the DFT geometry optimized structure of free-base **FP**. **d**, Hypothetical closure of the lower rim opening of **FP** with a quaternary carbon atom with a [5.5.5.5]fenestrane motif to give a non-IPR cage structure. **e**, Thermochemical analysis of the consecutive H_2 loss *via* cyclodehydrogenation of **1** to **FP**. Only isomers obtained from a zipper mechanism were considered (108 intermediates).

Sample preparation and general (S)TEM analysis. We drop-casted 10 μL of a 10^{-5} M solution of **1Pb** dissolved in THF on a dry-cleaned graphene-coated TEM grid, the excess solution was dabbed off, and the grid was dried in high vacuum (10^{-5} Pa) for 2 h before insertion into the TEM. Observations were carried out with an aberration-corrected TEM (JEM-ARM200F) at 303±5 K at magnifications of 1000k, equipped with a scintillator-based CMOS camera (Gatan OneView). The vacuum of the specimen chamber was constant at $1x10^{-5}$ Pa, the acceleration voltage was set to 80 kV, and the camera frame rate was kept at 2 fps. Traces of remaining volatiles were removed in the TEM by heating the grid to 473 K for 1 h before exposure to the electron beam. After scanning the graphene surface for viable candidates, we discovered a spherical structure attached to a graphene monolayer (GML) near an amorphous aggregate of Pb atoms, which served as a Pb-atom reservoir (Fig. 2a). Nearby, several single Pb-atoms were found to diffuse at the edge of the amorphous carbon layer. As shown in the high-angle annular dark-field scanning transmission electron microscopy (HAADF-STEM) images in Fig. 2b, the sizes of the Pb aggregates span from 2 to 25 nm while maintaining only minor crystalline character. Energy-dispersive X-ray spectroscopy (EDS) and mapping confirmed that the clusters consist of Pb atoms and are no other metal artifacts from sample preparation or the fabrication of the gold grid. On the other hand, the expected π–π stacks of pristine **1Pb**, demetalated **1**, or even immobilized structures *via* C–C bonds to graphene were not observed (Fig. 2c), since all molecules appeared to have reacted before being imaged by the primary beam electrons (*vide infra*).

The sheer number of single Pb-atoms and aggregates is astonishing. However, it can be rationalized by a hot electron ($E_{kin} > 0$ eV) reduction mechanism,[26,27] as described in Fig. 2c: An electron attachment to **1Pb** occurs through secondary electrons ($E_{kin} << 50$ eV)[28] from the specimen in the outer periphery of the electron beam-irradiated area, herein defined as beam shadow. Then, the metal ion is quickly released (order of picoseconds) from the macrocycle onto the substrate *via* an electrochemical reduction of $\mathbf{1Pb}^{0}$ to $\mathbf{1Pb}^{-1}$ or $\mathbf{1Pb}^{-2}$. Albeit a less common technique, wet-chemical reductive demetallation of porphyrins has been reported in the literature.[29,30] Evidence for the secondary electron accumulation in the beam shadow is visualized in the low magnification TEM image in Fig. 2d, in which the previously irradiated area at high magnification (highlighted with yellow arrows) is surrounded by a dark rim of charge-induced volatiles accumulation. Ejection and accumulation of secondary electrons from poorly conductive specimens are known

as the Berriman effect and are,[31–33] in our case, primarily driven by the poorly conductive hydrocarbon residues and amorphous carbon layers on the graphene surface. This effect leads to the net formation of an oxidative area, caused by the fast primary electrons from the beam, and a reductive site, induced by slow secondary electrons from the specimen, which is approximately 50 nm larger in diameter than the initial irradiated area.[34] Thus, the induced electric field is dependent on the conductivity of the specimen and the electron flux, as described in Fig. 2d iii-iv.[35]

A reductive demetallation mechanism is further supported by density functional theory (DFT) calculations, in which we determined the relative threshold dissociation energy ΔE_d for the Pb release from the macrocycle. As shown in Fig. 2e, reducing **1Pb^0** to **1Pb^{-1}** or **1Pb^{-2}** lowers ΔE_d(N_4-Pb) up to 1.7 eV, whereas an oxidative electron removal shows only marginal effects on the binding energy. Thus, the reductive demetallation is likely to proceed in the beam shadow without being witnessed by the direct microscopic observation, whereas a knock-on induced carbon displacement and thus the decomposition of macrocycle **1** is expected to proceed after a total electron dose (TED) of around 45 x 10^6 $e^- nm^{-2}$ and therefore renders this pathway to be unlikely (compare Extended Data Table 1). Identical observations were made for strongly complexed metal derivatives **1Pt**, **1Pd**, and **1Ni** (compare Extended Data Fig. 2), which describes this phenomenon as applicable beyond weakly bound Pb-porphyrins.

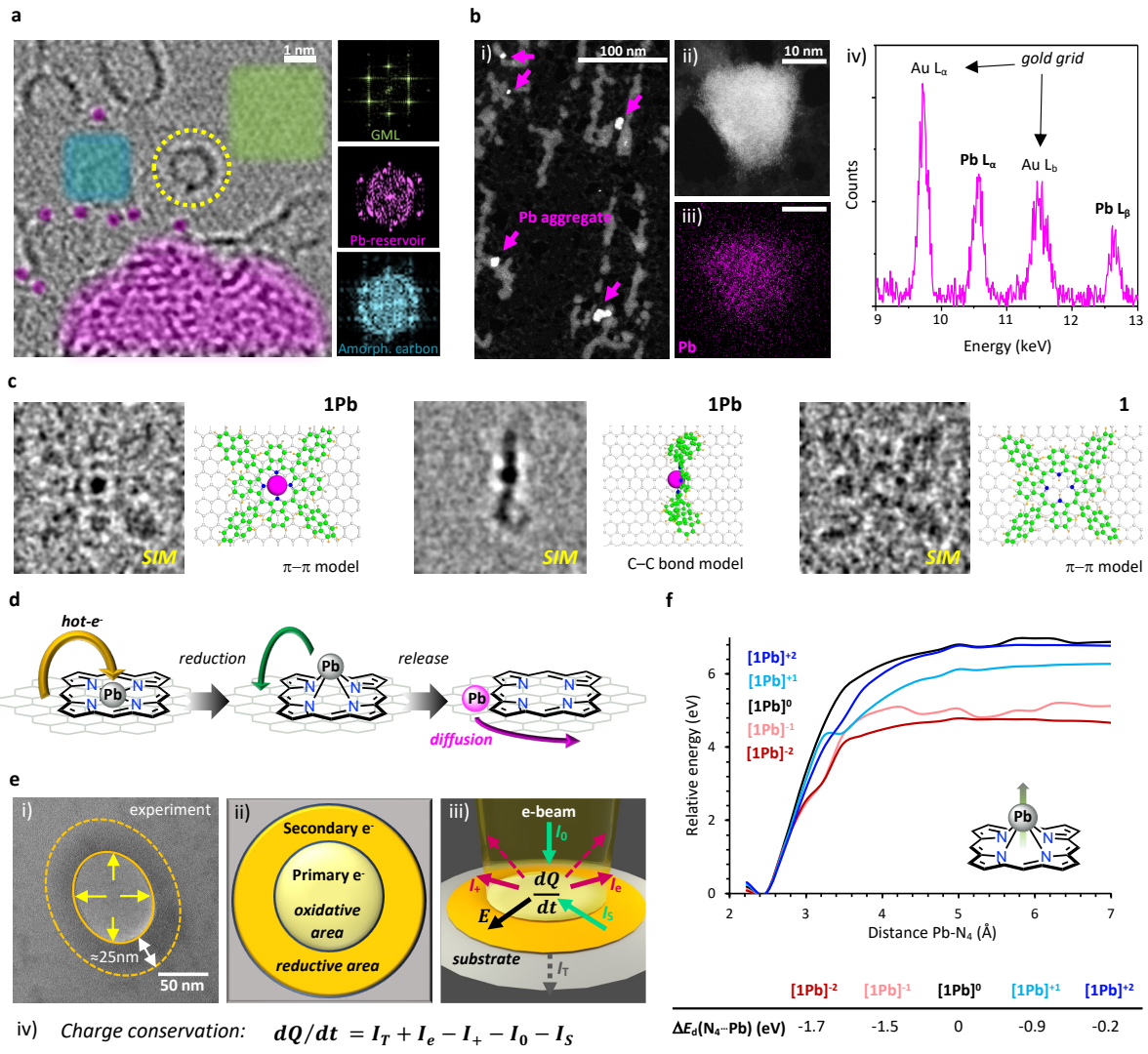

	[1Pb]$^{-2}$	[1Pb]$^{-1}$	[1Pb]^{0}	[1Pb]$^{+1}$	[1Pb]$^{+2}$
ΔE_d(N$_4$···Pb) (eV)	-1.7	-1.5	0	-0.9	-0.2

Fig. 2 Electron microscopic analysis of the overall environment of the starting FP intermediate and mechanistic insights. a, Overview of starting scene. The yellow dashed circle highlights the structure of interest; the magenta-highlighted area resembles an amorphous Pb-atom aggregate; the green area the GML; the blue area an amorphous carbon layer. The colors of the FFT diffraction pattern match the selected areas. **b**, HAADF-STEM image and EDS analysis of Pb-atom aggregates: i) low-mag. HAADF-STEM, ii) high-mag. HAADF-STEM, iii) EDS elemental mapping of Pb from ii), iv) EDS spectrum. **c**, TEM simulations of pristine **1Pb** and **1** on graphene. **d**, Proposed mechanism: 1) hot electron uptake; 2) reduction of metalloporphyrin; 3) decomplexation and release of metal atom onto the substrate. **e**, i) Berriman effect-induced accumulation of charged volatiles in the periphery of the primary beam-irradiated area, ii) beam-induced electrochemical areas on the substrate, iii) beam-induced currents on the substrate, iv) charge conservation equation; I_0: Primary electron beam current, I_T: transmitted electron beam current, E: electric field vector, I_e: secondary electron current, I_+: cation flux, I_S: electron back current. **f**, Morse potential for the N_4–Pb bond elongation and determination of the bond threshold dissociation energy E_d at different charging states of **1Pb**; calculated at the density functional B3LYP/6-31G(d)/LANL2DZ>Kr level of theory.

SMART-EM analysis. With the localized structure of interest from Fig. 2a, we will now focus on the structure determination and its dynamics during the course of observation (Supplementary Video 1). At this point, the time is arbitrarily set to 0 s, as the area might have been irradiated for 3-5 s during the search for the structure prior to the recording. Thus, the received energy from the e-beam transformed **1Pb** already into a cylindrical bowl structure, as reconstructed from the atomic number (*Z*)-adjusted model and TEM image simulations in Fig. 3a.[36] From statistical measurements of that singular entity over all frames ($t = 0$ s – 7.0 s) whose circular shape persisted, the structure measured 0.89 ± 0.02 nm x 0.90 ± 0.03 nm. These dimensions, shape, and phase contrast are well reproduced by a $C_{100}H_6N_4$ model **(hemi-1')Pb** (for comparison: **1** = $C_{100}H_{54}N_4$), with 20 zipped-up C–C bonds, six remaining hydrogen atoms, and a Pb atom coordinated by carbon atoms at the lower rim. The remaining dangling carbon atoms are bound to the GML, which immobilizes the structure on the surface. During a short transition period ($t = 7.5 – 9.0$ s), the shape of **(hemi-1")Pb** morphs to a pentagon-shaped structure with a diameter of 0.87 ± 0.02 nm, which lasts for 2.0 s (Fig. 3b). The transition is accompanied by the loss of four hydrogen atoms, as identified by the model. The simulation with a diameter of 0.89 nm fits well within the experimental error of ± 0.02 nm.

In the period from 12.0 s to 20.5 s, several dynamic processes with severe impact on the structure take place. As displayed in Fig. 3c, a second Pb-atom, fueled from the neighboring Pb-cluster, attaches to the structure to give a **(hemi-1'")Pb_2** structure that appears to be tipped over onto the sidewall. The model suggests that an additional C–C bond has formed at this point. From there on (Fig. 3d), the structure undergoes a rolling translation of around 0.65 nm on the surface, which leads to the C–C bond formation of the last three remaining open *fjord* regions and the subsequent incorporation of both Pb atoms; one into the endohedral cavity and the second by complexation at the porphyrinic site of the skeleton.

This exotic bimetallic cage structure, denoted as **Pb@(FP-Pb)** (Fig. 3e), could be identified by an excellent match between the experimental TEM image (diameter: 0.79 ± 0.01 nm) and the simulation (0.79 nm). Furthermore, from comparative simulations, we could verify that the metal atom is not located outside the cage (compare Extended Data Fig. 3) and thus get detailed insights about rather rare molecular Pb–Pb interactions as found in the complex. As shown in the side-view of the model, the experimentally measured Pb-Pb distance of 3.0 Å fits a model that contains a Pb–Pb single bond of 3.01 Å. While not many reports on bimetallic Pb-complexes are available,

our results fit well with the averaged Pb–Pb distance of 2.94 Å, as determined by single-crystal X-ray diffraction of molecular organo-Pb complexes.[37] All attempts simulating the structure with different Pb–Pb bond orders and at different tilting angles of the whole structure did not resolve the experimental findings (compare Extended Data Fig. 4). With these findings, we conclude **Pb@(FP-Pb)** to be remarkable in three ways: 1) It is proof of the possibility of incorporating the functional porphyrin macrocycle into a fullerene-like carbon cage. 2) It is a bimetallic species that contains a metal atom in the endohedral cavity and another as part of the skeletal structure. Previously, metalated fullerenes were limited to either endohedral or exohedral complexes only.[38,39] 3) It shows that Pb atoms, which have never been found in metallofullerenes before, can be incorporated into fullerene-like nanocages. Thus, in principle, other metal nanocages can be envisioned to be synthesized from similar bottom-up methodologies as well, which are unavailable at the moment *via* the standard arc-discharge techniques to endohedral metallofullernenes.[38]

In the last period of the movie (t = 31.5 – 43.5 s) in Fig. 3f, after a rotation of the structure, the skeletal Pb atom is ejected to leave a monometallic endohedral fullerophyrin **Pb@(FP)** behind, which remains stable under the imaging conditions for 12 s until the end of the movie. Again, this observation is significant as it proves the skeletal structure from another perspective and simultaneously highlights the envisioned reversibility of metallic complexation by the skeletal porphyrin. Furthermore, it qualitatively depicts the weakened Pb–Pb bond strength, which is indicated by the slightly increased bond length by 0.1 Å due to a reduced pyramidal inward coordination of the skeletal Pb atom. A vertically aligned structure of **Pb@(FP-Pb)**, in which the Pb atoms are placed atop of each other is unlikely, as evinced from a cross-correlation analysis of **Pb@(FP)** with **Pb@(FP-Pb)**, in which the cage structure shows poor overlap (Fig. 3g).

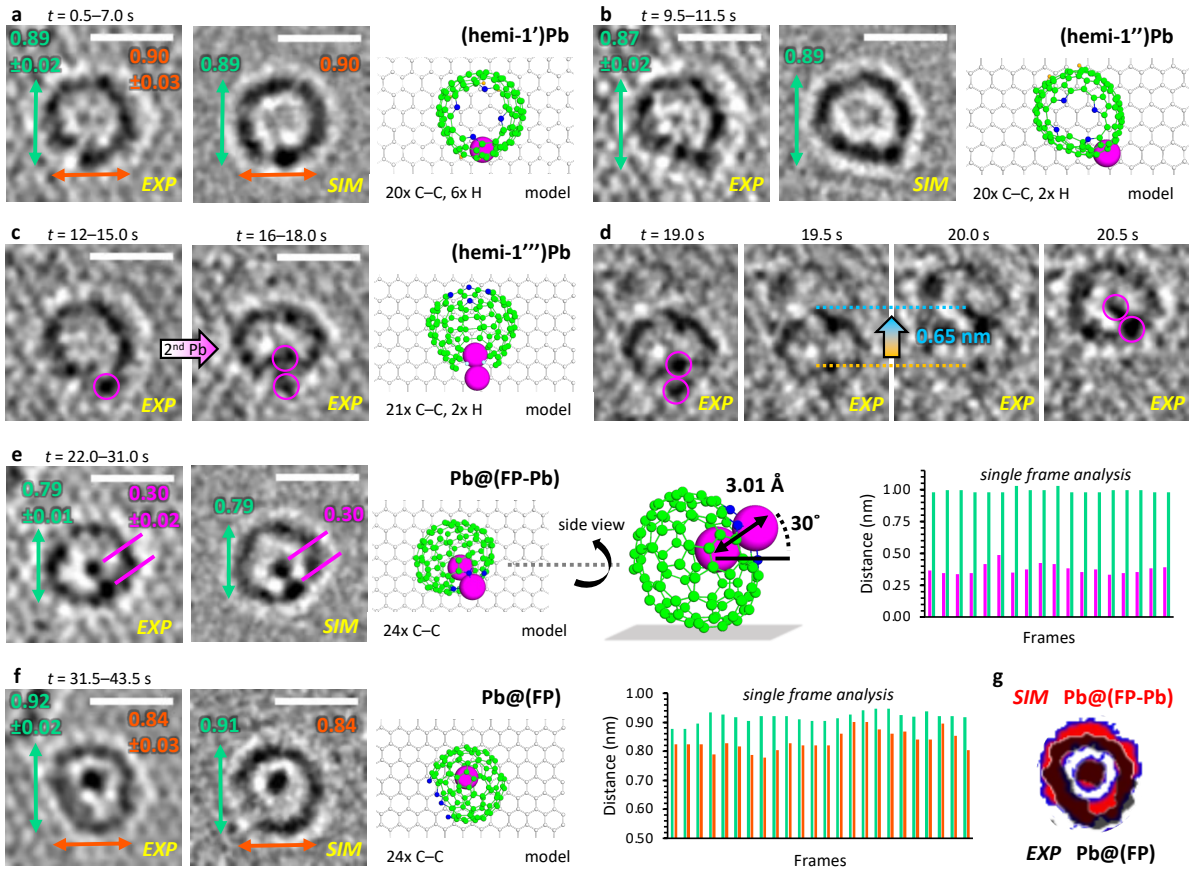

Fig. 3. SMART-EM Analysis of the FP formation. a, state of **(hemi-1')Pb** during the first 7 s; structure appears to have 20 closed C–C bonds and 6 remaining H atoms; dangling C atoms are bound to the surface. **b**, intermediate **(hemi-1")Pb** with morphed shape; 20 closed C–C bonds and 2 remaining H atoms. **c**, transition from a stationary structure to a pitched structure with an additional Pb atom **(hemi-1'")Pb_2**. **d**, apparent rolling of the structure over the surface. **e**, structural analysis of **Pb@(FP-Pb)**; all 24 C–C bonds closed, no remaining H atoms. **f**, Structural analysis of **Pb@(FP)**. **g**, Cross-correlation image of a simulated **Pb@(FP-Pb)** (red/blue) with vertically alligned Pb atoms and observed **Pb@(FP)** (black/white). Scale bar 1 nm.

Deconvolution of SMART-EM results. All chemical transformations are collected in a time-dependent event graph to assemble all factors and observations into a bigger picture (Fig. 4a). As depicted, the electron dose rate (EDR) of around 1.5 x 10^6 e^- nm^2s^{-1} remains nearly constant over the whole period, which leads to a linear accumulation of the TED over time. However, the observed molecular events show no linear correlation between the TED and EDR and thus appear stochastically. Nonetheless, each process, such as an H atom loss or C–C bond formation, can be correlated to a translational event of the structure on the surface.[20] A mere knock-on induced C–C bond formation *via* hydrogen atom shedding to C• radicals, followed by radical recombination, can be ruled out for three reasons: 1) A significant energy contribution to the formation of the first hemi-fullerophyrin **(hemi-1')Pb** must have come already from secondary electrons in the beam shadow while scanning the area. The secondary electron flux derived from the carbon substrate at our experimental conditions is estimated to be 5.7 x 10^3 e^- $nm^{-2}s^{-1}$. However, they cannot transfer enough momentum for a homolytic C–H bond cleavage due to their reduced kinetic energy (typically <<50 eV). As shown in Fig. 4b, a minimum kinetic energy of 3500 eV is required for a knock-on induced C–H bond cleavage in **1Pb**, yet even fast secondary electrons from an inner shell oxidation of the specimen do not reach the required energy (carbon K-shell (1s) = 284 eV).[28] Nonetheless, their kinetic energy can be sufficiently low for electron attachment-induced processes, such as the hot electron reduction (*vide supra*) or a reductive cyclodehydrogenation.[40–42] 2) The knock-on displacement cross-section σ_d, derived from the McKinley-Feshbach equation,[13] indicates that the earliest event of H atom shedding under direct 80 keV e-beam irradiation should occur for **1Pb** after 19 x 10^6 e^- nm^{-2}. However, even if a maximum additional irradiation time of 5 s in the pre-recording period is considered, the loss of >80% of the H atoms in **1Pb** cannot be explained. This finding indicates that the processes observed in this video are a result of a less energy-demanding chemical reaction mechanism rather than a physical fragmentation of the molecule *via* knock-on displacement.[20] This includes the demetallation of **1Pb** *via* secondary knock-on effects from fast H-atoms, which cannot overcome the threshold displacement energy of complexed Pb of around 6 eV with a maximum transferred kinetic energy of $E_{T'}$ = 3.60 eV (compare Extended Data Fig. 5). 3) The significantly larger ionization cross-section of the highest occupied molecular orbital (HOMO) σ_{rBEB} by a factor of 10^5, derived from the relativistic Binary-Encounter-Bethe model,[43] suggests that the observed transformations such as the demetallation and cyclodehydrogenation reactions are redox-based processes and thus, can

be regarded as electron beam-induced electrochemical analogs to the respective wet-chemical reactions.

Another observation that can be reasoned with quantum chemical rationale is the fixation of the molecule to the graphene surface at the most-curved outer sidewall. A van der Waals-based immobilization of the molecule would prefer interactions with a larger surface area, subsequently leading to different TEM images (compare Extended Data Fig. 6). However, analogously to the reactivity of strained double bonds in fullerenes,[44,45] the π-bond polarization resulting from the skeletal curvature facilitates the bonding to the GML *via* cycloaddition reactions. This is visualized with the electrostatic potential (ESP) map of **Pb@(FP-Pb)** (Fig. 4c), which shows the strongest polarization compared to **FP** or **Pb@(FP)** (compare Extended Data Fig. 7a). In view of the frontier molecular orbitals and therefore the cycloaddition chemistry of fullerophyrins, metalation of **FP** lifts the energy level of the highest occupied molecular level (HOMO), which is located at the outer curvature of the cage, while the lowest unoccupied molecular orbital (LUMO) remains nearly unaffected (Fig. 4d). Ionization on the other hand, is dominated by the soft metal atoms of **Pb@(FP)** and **Pb@(FP-Pb)** (Fig 4e, and Extended Data Fig. 7b).

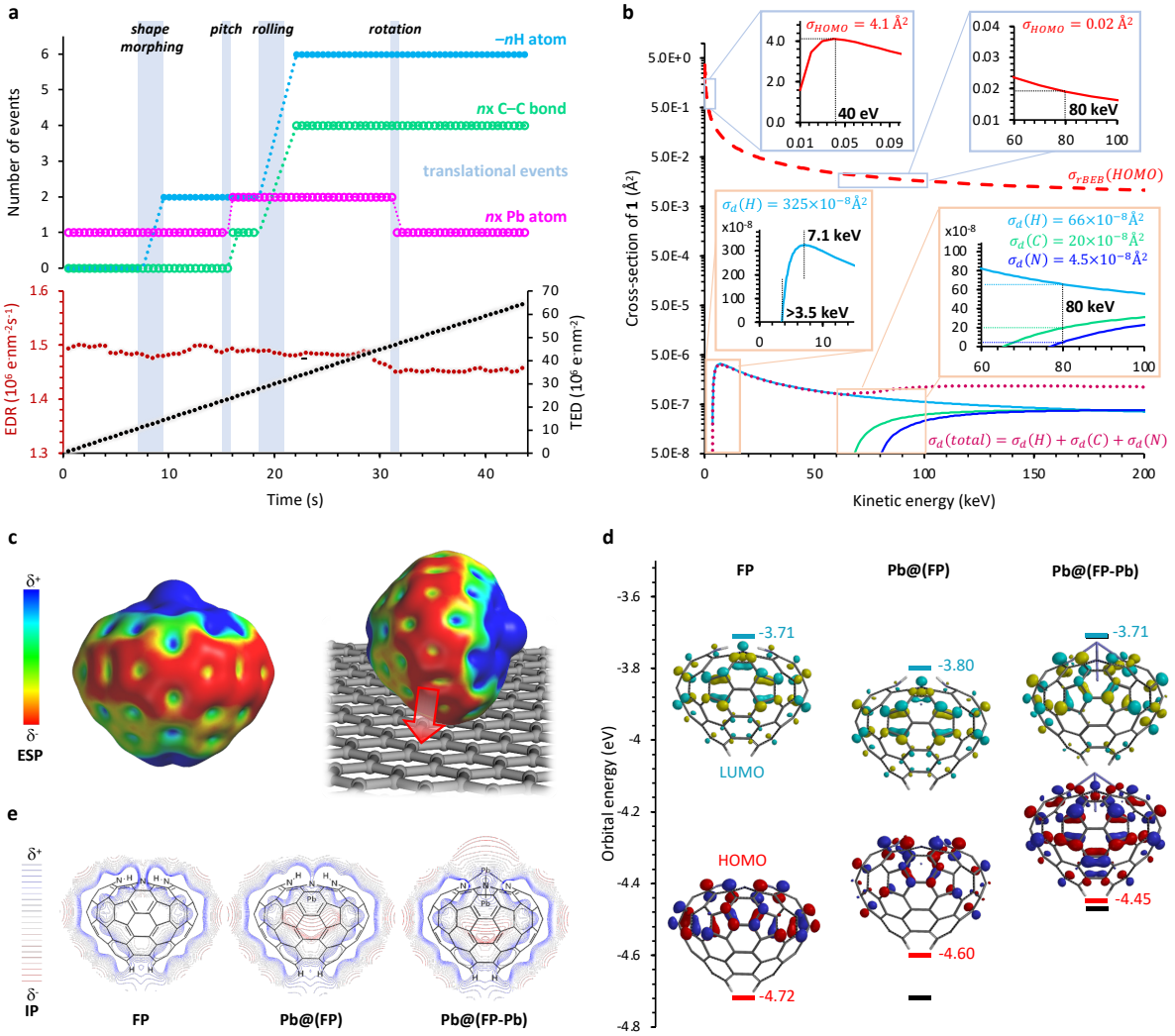

Fig. 4. Summary of events and electronic characteristics of fullerophyrins. a, Number of events, total electron dose (TED), and electron dose rate (EDR), plotted against the time. **b**, Theoretical ionization cross-section (σ_{rBEB}) of **1**(HOMO) and knock-on displacement cross-section (σ_d) for H, C, and N atoms calculated for **1**. **c**, Electrostatic potential map of **Pb@(FP-Pb)** (color range from -30 to +20 kJ/mol, isovalue 0.002 e/au³). **d**, Energy distribution of frontier molecular orbitals of **FP**, **Pb@(FP)**, and **Pb@(FP-Pb)** (isovalue 0.032 $\sqrt{}$ (e/au³)). **e**, Sliced contour plot of the ionization potential of **FP**, **Pb@(FP)**, and **Pb@(FP-Pb)** (color range from 8 to 15 eV). DFT level: B3LYP-D3/6-31G(d)/LANL2DZ>Kr.

Conclusion

Although first studies of matter under the influence of radiation can be dated back to the 19th century,[46] the understanding of fast electron-induced molecular reactions is still in its infancy. Enabled through the radiation chemical cyclodehydrogenation, we demonstrated the transformation of a benzoporphyrin precursor **1Pb** to a designer-made doubly-holed fullerene-porphyrin cage structure **FP** by in-depth SMART-EM analysis. Simultaneously, we evidenced the ability of **FP** to host up to two Pb atoms, which led to the exotic formation of bimetallic **Pb@(FP-Pb)** and the monometallic endohedral **Pb@(FP)**. Subsequent insights about the complexation dynamics and the Pb–Pb binding motif of this organometallic cage structure were obtained. From the observations, we conclude that not only the fast primary electrons have to be considered for chemical transformations, but also the much slower secondary electrons in the beam shadow. The latter electron species might be responsible for the demetalation of the porphyrins *via* a hot-electron reduction, as well as the partial C–C bond formation to **(hemi-1')Pb** *via* a reductive cyclodehydrogenation. In contrast, the final cyclodehydrogenation reaction to the strained fullerene-like cage structure occurs under an oxidative primary 80 kV beam. With these cinematographic insights, we believe that SMART-EM will serve not only as an analytical tool for physical organic chemists but will resolve the synthetic capacity that can be expected from focused electron beam-induced reactions. Consequently, understanding radiation chemistry on the molecular level will tremendously impact the design and fabrication of well-defined topological nanostructures by e-beam lithographic techniques.[35,47]

Online Content

The authors declare that the data supporting the findings of this study are available within the paper and its supplementary information files.

Supporting Information. The following files are available free of charge. PDF file (Captions for Video S1 to S3, Supplementary Synthetic Details, Supplementary Description of Cross-Section Calculation, Supplementary Computational Details, XYZ Coordinates, NMR and MS Spectral Appendix, Supplementary Text, Figures S1 to S36, Supplementary Tables S1 to S19, Supplementary References), and AVI video files (Video S1 to S3).

Methods

General synthetic methods. Chemicals were purchased from Sigma-Aldrich and used without further purification. Solvents were distilled prior to usage. CH_2Cl_2 was neutralized with K_2CO_3 prior to distillation. Et_2O was dried over CaH_2 and distilled prior to usage. Reactions were carried out under a dry N_2 or Ar atmosphere, using standard Schlenk techniques. Further synthetic details are described in the Supplementary Information.[48]

Synthesis of 1. Pyrene-2-carbaldehyde **3** (0.489 g; 2.12 mmol) and 4,7-dihydro-2*H*-ethanoisoindole **2** (0.307 g; 2.11 mmol) were dissolved in CH_2Cl_2 (125 mL) in a 250 mL Schlenk flask under N_2. The solution was purged with N_2 for 15 min before $BF_3{\cdot}OEt_2$ (0.075 mL, 0.61 mmol) was added. The mixture was stirred for 20 h at rt under light exclusion. Then DDQ (0.475 g; 2.09 mmol) was added, and the mixture was brought to reflux for 2 h under N_2. After cooling to rt, the mixture was washed with a solution of 10% aqueous Na_2SO_3 (125 mL) and 10% Na_2CO_3 (125 mL). The phases were separated, and the solvent was removed under vacuum. Then the crude product was heated under vacuum to 200 °C for 1.5 h. After cooling to rt, the solid was dissolved in CH_2Cl_2 and purified by plug filtration (SiO_2, diameter 4 cm; height: 8 cm; CH_2Cl_2 + 1% TFA). The final purification was carried out by recrystallization ($MeOH/CH_2Cl_2$). The product was isolated as a dark green solid in 81% yield (0.565 g; 0.431 mmol).[49–51]

Synthesis of 1Pb. In a flame-dried Schlenk tube, $Pb(OAc)_2x3H_2O$ (22 mg; 57 μmol, 15 equiv) was dissolved in DMF (1.0 mL) under N_2 and heated to 135 °C for 5 min. 5,10,15,20-tetrakis(2-pyrenyl)tetrabenzoporphyrin **1** (5.0 mg; 3.8 μmol) was added, and the mixture was heated to 140 °C for 2 h. The reaction was cooled to rt, and the solvent was removed in vacuum. The crude product was re-dissolved in a small amount of CH_2Cl_2 and precipitated with MeOH. The precipitate was filtered and washed several times with MeOH. The brownish, slightly purple product (around 4 mg) was collected and stored in the vacuum on a hydrophobic PTFE filter paper until used for TEM experiments.

Synthesis of 2. 4,7-dihydro-2*H*-ethanoisoindole **2** was prepared according to a procedure by Ruppel *et al*. Spectral data agreed with respective literature data.[49]

Synthesis of 3. 2-Bromopyrene **4** (1.0 g, 3.56 mmol) was suspended in Et_2O (50 mL) under N_2 in a 250 mL Schlenk flask and cooled to -20 °C (ice water/salt mixture). *n*-BuLi 1.6 M in hexanes (5.0 mL, 8.0 mmol, 2.2 equiv) was added slowly under N_2, and the reaction mixture was stirred for 1h at -20 °C. Then the bath was removed, and the mixture was stirred for another 30 min at rt. After the addition of DMF (10 mL, 144 mmol, 40 equiv), the mixture was stirred for 1 h at rt. The reaction was quenched carefully with 10% HCl solution, and the organic layer was evaporated. The mixture was extracted with CH_2Cl_2 (2x150 mL), and the combined organic layers were washed with water (2x150 mL) and brine (150 mL) before they were dried over $MgSO_4$ and filtered. The solvent was removed by rotary evaporation. The crude product was adsorbed on silica gel and purified *via* column chromatography (SiO_2, diameter: 5 cm, height: 30 cm, CH_2Cl_2:hexanes = 3:2). The product was isolated as a pale-yellow solid in 53% yield (0.43 g, 1.87 mmol).

Synthesis of 4. 2-bromopyrene **4** was synthesized according to a procedure by Crawford *et al*. Spectral data agreed with respective literature data.[52]

TEM grid preparation. CVD-grown monolayer graphene-coated quantifoil gold-grids, with a hole size of 2 μm and space between the holes of 4 μm, were purchased from Graphenea. Prior to usage, the graphene grids were purified with activated carbon using a modified dry-cleaning protocol.[20,53] A small amount of dried activated carbon was placed into a petri dish, and the graphene grid was carefully placed atop and then fully covered with another portion of activated carbon. The petri dish was placed in a furnace under ambient conditions and annealed: 1) rt to 210 °C in 45 min (heating rate around 4.6°C/min); 2) 210 °C for 30 min; 3) cooling to 120 °C in 30 min. The grid was stored at 120 °C under activated carbon until it was used for the sample preparation. The grid was then mechanically cleaned from the activated carbon, using a gentle stream of dry N_2 for several minutes.

Sample preparation. A 10^{-5} M solution of **1Pb** (10 μL) in THF was freshly prepared by dissolving the solid from the PTFE filter paper in THF (3 mL) before drop-casting one drop onto the dry-cleaned graphene grid. The excess sample solution was removed with a filter paper. The sample grid was cleaned with two cycles of MeOH (10 μL), followed by the removal of excess solvent with a filter paper. The grid was then pre-dried in high vacuum at 5×10^{-5} Pa for 2 h before introducing the sample into the TEM chamber.

SMART-EM, STEM, and EDS elemental mapping. Observations were carried out on a cold FEG JEOL JEM-ARM200F instrument, equipped with a Cs aberration corrector and JED-2300T Energy Dispersive X-ray Spectrometer, at an acceleration voltage of 80 kV and a vacuum of 1×10^{-5} Pa in the specimen chamber. Experiments were carried out on a heating holder (JEOL EM-21130). To remove volatile impurities from the specimen, the holder was heated at 573 K for 30–60 min without electron irradiation before cooling to 298 ± 5 K. After the stage temperature settled to the target value, we waited for an additional 30 min to minimize thermal drift. EM videos were recorded on a CMOS camera (Gatan OneView, 4,096 × 4,096 pixels) operated in binning 2 mode (output image size: 2,048 × 2,048 pixels, pixel resolution 0.021 nm at ×1000,000), with an exposure time of 500 ms and a framerate of 2 fps. All images were automatically processed on Gatan DigitalMicrograph software. The specimen was screened for viable candidates at low dose conditions ($\approx 10^{-5}$ $e^{-}s^{-1}nm^{-2}$) to suppress e-beam-induced processes as much as possible. The typical time between finding and starting the recording of a respective scene was 1 to 3 s. STEM and EDS elemental mapping were carried out on a beryllium holder (JEOL EM-21130) at room temperature. HAADF STEM detector was used with a camera length of 8 cm (with detection angles ranging from 68 to 280mrad). The Probe size was 7C (60 pA), and the CL aperture size was 40 μm. The probe convergence angle was X (something between 28 to 33mrad).

Image processing. Images were collected in the .dm3 format on Gatan DigitalMicrograph software and processed using ImageJ 1.51f software.[54] To remove the unevenness of the electron irradiation, all images were processed by a bandpass filter (filtering structures smaller than 3 pixels and larger than 40 pixels, tolerance of direction: 5%), and contrast/brightness adjusted. Prior to analysis, images were subjected to a thermal drift correction. TEM simulation images were corrected according to the TEM experiment's electron dose rate and generated using a multi-slice procedure implemented in the Bionet elbis software.[55] Simulation parameters were set to agree with the actual experimental parameters: acc. Volt. = 80.00 kV, λ = 0.04176 Å, Cs = -0.003 mm, df = 120 Å, Cc = 1.25 mm, de = 0.60 eV, α = 0.20 mrad, OL Aperture radius = 20.88 mrad, OL Aperture radius = 0.50 $Å^{-1}$, pixel size = 0.0210844, max. Intens. = 1.1278. The simulations were processed analogously to the experimental TEM images to obtain the best correlation.

Single-molecule statistical analysis. Single-molecule statistics were carried out from the plot profile analysis of the observed intermediate structures. The black maxima in the profile were used and measured as a reference point. The standard deviation was calculated according to Eq. 1.

$$\sigma = \sqrt{\frac{\sum_{i=1}^{n}(x_i - \bar{x})^2}{n-1}} \quad \text{Eq. 1}$$

DFT calculations. Geometry optimization and energy calculations were performed on Q-Chem as implemented in the SPARTAN '20 work package.[56,57] Structures were optimized using the Head Gordon range-separated global hybrid generalized gradient approximation functional ωB97X-D with Grimme D2 dispersion correction.[58] Geometry optimization and initial evaluation of the molecules' energies were performed with the Pople-type dual basis split-valence triple-ζ/double-ζ quality basis set 6-311G(d,p)[6-31G(d)]. Thermochemical calculations were obtained using the Minnesota global hybrid meta generalized gradient approximation functional M06-2X with 54% Hartree-Fock exchange[59] in combination with the Ahlrichs-Weigend triple-ζ quality basis set def2-TZVP.[60] Further computational details and the calculations of cross-sections using the McKinley Feshbach approximation and the relativistic Binary encounter Bethe model are described in the Supplementary Information.

Acknowledgement

The research was supported by the Institute for Basic Science (IBS-R026-Y1, IBS-R026-D1), JSPS (KAKENHI JP19H05459), Japan Science and Technology Agency (CREST JPMJCR20B2), and the Deutsche Forschungsgemeinschaft (DFG, Projektnummer 182849149, SFB 953). H.H. and D.L. acknowledge the support as an International Research Fellow from the Japan Society for the Promotion of Science (JSPS). H.H. further thanks the Bavarian Equal Opportunities Sponsorship – Realisierung von Chancengleichheit von Frauen in Forschung und Lehre (FFL) – Realization Equal Opportunities for Women in Research and Teaching, for financial support. D.L. further thanks the Alexander von Humboldt Foundation (AvH) for a Feodor-Lynen return fellowship.

Author Contributions

D.L. conceptualized the project and wrote the manuscript with feedback from all authors. All authors discussed the results and commented on the manuscript. N.J. and K.Y.A. designed the molecule. H.H. synthesized and characterized the molecules. H.H. and D.L. carried out the TEM experiments. S.L. carried out the STEM/EDS experiments and analysis. D.L. carried out SMART-EM data analysis, DFT calculations, and EM simulations. K.H. and E.N. provided access and maintenance of the TEM. E.N., N.J., and D.L. were responsible for funding acquisition. All authors approved the final version of the manuscript.

Competing Interests statement

The authors declare no competing interests.

References

1. Nakamura, E. Atomic-Resolution Transmission Electron Microscopic Movies for Study of Organic Molecules, Assemblies, and Reactions: The First 10 Years of Development. *Acc. Chem. Res.* **50**, 1281–1292 (2017).

2. Skowron, S. T. *et al.* Chemical Reactions of Molecules Promoted and Simultaneously Imaged by the Electron Beam in Transmission Electron Microscopy. *Acc. Chem. Res.* **50**, 1797–1807 (2017).

3. Nakamuro, T., Sakakibara, M., Nada, H., Harano, K. & Nakamura, E. Capturing the Moment of Emergence of Crystal Nucleus from Disorder. *J. Am. Chem. Soc.* **143**, 1763–1767 (2021).

4. Xing, J., Schweighauser, L., Okada, S., Harano, K. & Nakamura, E. Atomistic structures and dynamics of prenucleation clusters in MOF-2 and MOF-5 syntheses. *Nat. Commun.* **10**, 3608 (2019).

5. Nakamuro, T. *et al.* Time-Resolved Atomistic Imaging and Statistical Analysis of Daptomycin Oligomers with and without Calcium Ions. *J. Am. Chem. Soc.* **144**, 13612–13622 (2022).

6. Biskupek, J. *et al.* Bond Dissociation and Reactivity of HF and H2O in a Nano Test Tube. *ACS Nano* **14**, 11178–11189 (2020).

7. Cao, K. *et al.* Imaging an unsupported metal–metal bond in dirhenium molecules at the atomic scale. *Sci. Adv.* **6**, eaay5849 (2020).

8. Jordan, J. W. *et al.* Single-molecule imaging and kinetic analysis of intermolecular polyoxometalate reactions†. *Chem. Sci.* **12**, 7377–7387 (2021).

9. Cao, K. *et al.* Atomic mechanism of metal crystal nucleus formation in a single-walled carbon nanotube. *Nat. Chem.* **12**, 921–928 (2020).

10. Kharel, P. *et al.* Atomic-Resolution Imaging of Small Organic Molecules on Graphene. *Nano Lett.* **22**, 3628–3635 (2022).

11. Mirzayev, R. *et al.* Buckyball sandwiches. *Sci. Adv.* **3**, e1700176 (2017).

12. Choe, J. *et al.* Direct imaging of structural disordering and heterogeneous dynamics of fullerene molecular liquid. *Nat. Commun.* **10**, 4395 (2019).

13. Susi, T., Meyer, J. C. & Kotakoski, J. Quantifying transmission electron microscopy irradiation effects using two-dimensional materials. *Nat. Rev. Phys.* **1**, 397–405 (2019).

14. Cai, Z., Chen, S. & Wang, L.-W. Dissociation path competition of radiolysis ionization-induced molecule damage under electron beam illumination. *Chem. Sci.* **10**, 10706–10715 (2019).

15. Egerton, R. F. Radiation damage to organic and inorganic specimens in the TEM. *Micron* **119**, 72–87 (2019).

16. Liu, D. *et al.* Ionization and electron excitation of C_{60} in a carbon nanotube: A variable temperature/voltage transmission electron microscopic study. *Proc. Natl. Acad. Sci.* **119**, e2200290119 (2022).

17. Chamberlain, T. W. *et al.* Isotope Substitution Extends the Lifetime of Organic Molecules in Transmission Electron Microscopy. *Small* **11**, 622–629 (2015).

18. Okada, S. *et al.* Direct Microscopic Analysis of Individual C60 Dimerization Events: Kinetics and Mechanisms. *J. Am. Chem. Soc.* **139**, 18281–18287 (2017).

19. Shimizu, T., Lungerich, D., Harano, K. & Nakamura, E. Time-Resolved Imaging of Stochastic Cascade Reactions over a Submillisecond to Second Time Range at the Angstrom Level. *J. Am. Chem. Soc.* **144**, 9797–9805 (2022).

20. Lungerich, D. *et al.* A Singular Molecule-to-Molecule Transformation on Video: The Bottom-Up Synthesis of Fullerene C_{60} from Truxene Derivative C60H30. *ACS Nano* **15**, 12804–12814 (2021).

21. Scott, L. T. *et al.* A rational chemical synthesis of C_{60}. *Science* **295**, 1500–1503 (2002).

22. Boorum, M. M., Vasil'ev, Y. V., Drewello, T. & Scott, L. T. Groundwork for a rational synthesis of C60: cyclodehydrogenation of a $C_{60}H_{30}$ polyarene. *Science* **294**, 828–831 (2001).

23. Chuvilin, A., Kaiser, U., Bichoutskaia, E., Besley, N. A. & Khlobystov, A. N. Direct transformation of graphene to fullerene. *Nat. Chem.* **2**, 450–453 (2010).

24. Cao, K. *et al.* Comparison of atomic scale dynamics for the middle and late transition metal nanocatalysts. *Nat. Commun.* **9**, 3382 (2018).

25. Lungerich, D. *et al.* Gas-Phase Transformation of Fluorinated Benzoporphyrins to Porphyrin-Embedded Conical Nanocarbons. *Chem. Eur. J.* **26**, 12180–12187 (2020).

26. Xie, W. & Schlücker, S. Hot electron-induced reduction of small molecules on photorecycling metal surfaces. *Nat. Commun.* **6**, 7570 (2015).

27. Kim, M., Lin, M., Son, J., Xu, H. & Nam, J. Hot-Electron-Mediated Photochemical Reactions: Principles, Recent Advances, and Challenges. *Adv. Opt. Mater.* **5**, 1700004 (2017).

28. Brydson, R. *Electron Energy Loss Spectroscopy*. (Taylor & Francis, 2001). doi:10.1201/9781003076858-1.

29. Kumar, M., Neta, P., Sutter, T. P. G. & Hambright, P. One-electron reduction and demetallation of copper porphyrins. *J. Phys. Chem.* **96**, 9571–9575 (1992).

30. Cowan, J. A. & Sanders, J. K. M. Reductive demetallation of porphyrins: Evidence for peripheral and axial modes of reduction. *Tetrahedron Lett.* **27**, 1201–1204 (1986).

31. Russo, C. J. & Henderson, R. Charge accumulation in electron cryomicroscopy. *Ultramicroscopy* **187**, 43–49 (2018).

32. Downing, K. H., McCartney, M. R. & Glaeser, R. M. Experimental Characterization and Mitigation of Specimen Charging on Thin Films with One Conducting Layer. *Microsc. Microanal.* **10**, 783–789 (2004).

33. Brink, J., Sherman, M. B., Berriman, J. & Chiu, W. Evaluation of charging on macromolecules in electron cryomicroscopy. *Ultramicroscopy* **72**, 41–52 (1998).

34. Kuei, B. & Gomez, E. D. Pushing the limits of high-resolution polymer microscopy using antioxidants. *Nat. Commun.* **12**, 153 (2021).

35. Gonzalez-Martinez, I. G. *et al.* Electron-beam induced synthesis of nanostructures: a review. *Nanoscale* **8**, 11340–11362 (2016).

36. Xing, J. *et al.* Atomic-number (Z)-correlated atomic sizes for deciphering electron microscopic molecular images. *Proc. Natl. Acad. Sci.* **119**, e2114432119 (2022).

37. Wang, Y., Quillian, B., Wei, P., Yang, X.-J. & Robinson, G. H. New Pb–Pb bonds: syntheses and molecular structures of hexabiphenyldiplumbane and tri(trisbiphenylplumbyl)plumbate. *Chem. Commun.* **0**, 2224–2225 (2004).

38. Popov, A. A., Yang, S. & Dunsch, L. Endohedral Fullerenes. *Chem. Rev.* **113**, 5989–6113 (2013).

39. Nakamura, E. Bucky ferrocene and ruthenocene: serendipity and discoveries. *J. Organomet. Chem.* **689**, 4630–4635 (2004).

40. Kawahara, K. P., Matsuoka, W., Ito, H. & Itami, K. Synthesis of Nitrogen-Containing Polyaromatics by Aza-Annulative π-Extension of Unfunctionalized Aromatics. *Angew. Chem. Int. Ed.* **59**, 6383–6388 (2020).

41. Wang, C., Sun, Q., García, F., Wang, C. & Yoshikai, N. Robust Cobalt Catalyst for Nitrile/Alkyne [2+2+2] Cycloaddition: Synthesis of Polyarylpyridines and Their Mechanochemical Cyclodehydrogenation to Nitrogen-Containing Polyaromatics. *Angew. Chem. Int. Ed.* **60**, 9627–9634 (2021).

42. Rickhaus, M., Belanger, A. P., Wegner, H. A. & Scott, L. T. An Oxidation Induced by Potassium Metal. Studies on the Anionic Cyclodehydrogenation of 1,1′-Binaphthyl to Perylene. *J. Org. Chem.* **75**, 7358–7364 (2010).

43. Kim, Y.-K., Santos, J. P. & Parente, F. Extension of the binary-encounter-dipole model to relativistic incident electrons. *Phys. Rev. A* **62**, 052710 (2000).

44. Stevenson, S. *et al.* Semiconducting and Metallic [5,5] Fullertube Nanowires: Characterization of Pristine D5h(1)-C90 and D5d(1)-C100. *J. Am. Chem. Soc.* **143**, 4593–4599 (2021).

45. Hirsch, A. & Brettreich, M. *Fullerenes*. (WILEY-VCH Verlag, 2005).

46. Kinchin, G. H. & Pease, R. S. The Displacement of Atoms in Solids by Radiation. *Rep. Prog. Phys.* **18**, 1 (1955).

47. Egerton, R. Radiation Damage and Nanofabrication in TEM and STEM. *Microsc. Today* **29**, 56–59 (2021).

48. Hölzel, H. *Hybrid architectures based on carbon-rich pi-systems and porphyrins*. (Friedrich-Alexander University Erlangen-Nuernberg, 2021).

49. Ruppel, M. *et al.* A Comprehensive Study on Tetraaryltetrabenzoporphyrins. *Chem. Eur. J.* **26**, 3287–3296 (2020).

50. Ruppel, M., Gazetas, L.-P., Lungerich, D., Hampel, F. & Jux, N. Investigations of Low-Symmetrical Tetraaryltetrabenzoporphyrins Produced by Mixed Condensation Reactions. *J. Org. Chem.* **85**, 7781–7792 (2020).

51. Ruppel, M., Gazetas, L.-P., Lungerich, D. & Jux, N. Synthesis and Photophysical Properties of Hexabenzocoronene-Tetrabenzoporphyrin Architectures. *Eur. J. Org. Chem.* **2020**, 6352–6360 (2020).

52. Crawford, A. G. *et al.* Synthesis of 2- and 2,7-Functionalized Pyrene Derivatives: An Application of Selective C–H Borylation. *Chem. Eur. J.* **18**, 5022–5035 (2012).

53. Algara-Siller, G., Lehtinen, O., Turchanin, A. & Kaiser, U. Dry-cleaning of graphene. *Appl. Phys. Lett.* **104**, 153115 (2014).

54. Schneider, C. A., Rasband, W. S. & Eliceiri, K. W. NIH Image to ImageJ: 25 years of image analysis. *Nature methods* **9**, 671–675 (2012).

55. Hosokawa, F., Shinkawa, T., Arai, Y. & Sannomiya, T. Benchmark test of accelerated multi-slice simulation by GPGPU. *Ultramicroscopy* **158**, 56–64 (2015).

56. Shao, Y. *et al.* Advances in molecular quantum chemistry contained in the Q-Chem 4 program package. *Molecular Physics* **113**, 184–215 (2015).

57. Shao, Y. *et al.* Advances in methods and algorithms in a modern quantum chemistry program package. *Physical Chemistry Chemical Physics* **8**, 3172–3191 (2006).

58. Chai, J.-D. & Head-Gordon, M. Long-range corrected hybrid density functionals with damped atom-atom dispersion corrections. *Physical Chemistry Chemical Physics* **10**, 6615–6620 (2008).

59. Zhao, Y. & Truhlar, D. G. The M06 suite of density functionals for main group thermochemistry, thermochemical kinetics, noncovalent interactions, excited states, and transition elements: Two new functionals and systematic testing of four M06-class functionals and 12 other functionals. *Theoretical Chemistry Accounts* **120**, 215–241 (2008).

60. Weigend, F. & Ahlrichs, R. Balanced basis sets of split valence, triple zeta valence and quadruple zeta valence quality for H to Rn: Design and assessment of accuracy. *Physical Chemistry Chemical Physics* **7**, 3297–3305 (2005).

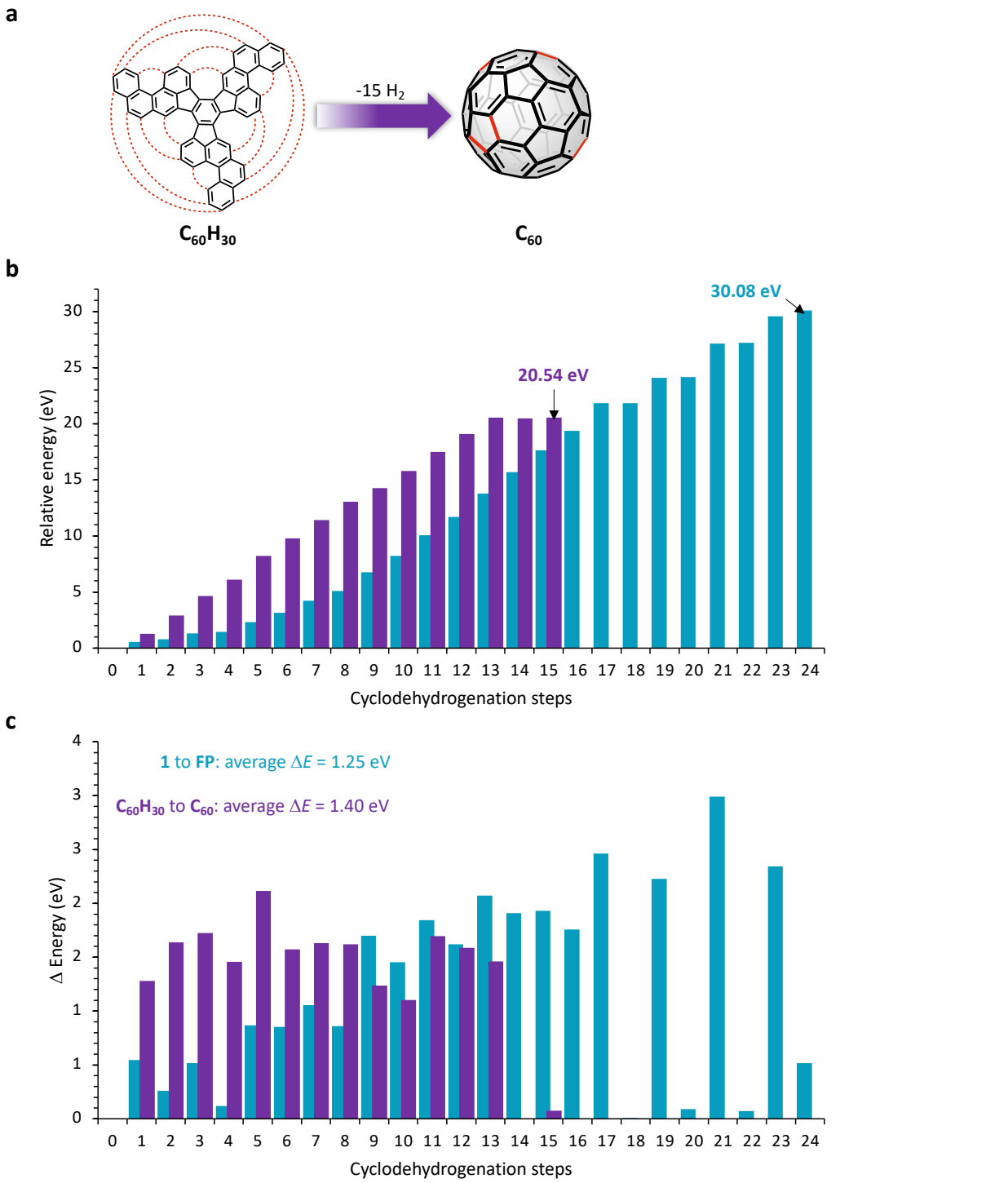

Extended Data Fig. 1. Thermochemical comparison of the cyclodehydrogenation reaction of $C_{60}H_{30}$ to C_{60} and 1 to FP. a, Reaction equation for the $C_{60}H_{30}$ to C_{60} conversion. **b**, Relative energies of intermediates for each reaction. **c**, Energy difference between each reaction intermediate. (DFT: M06-2X/def2-TZVP).

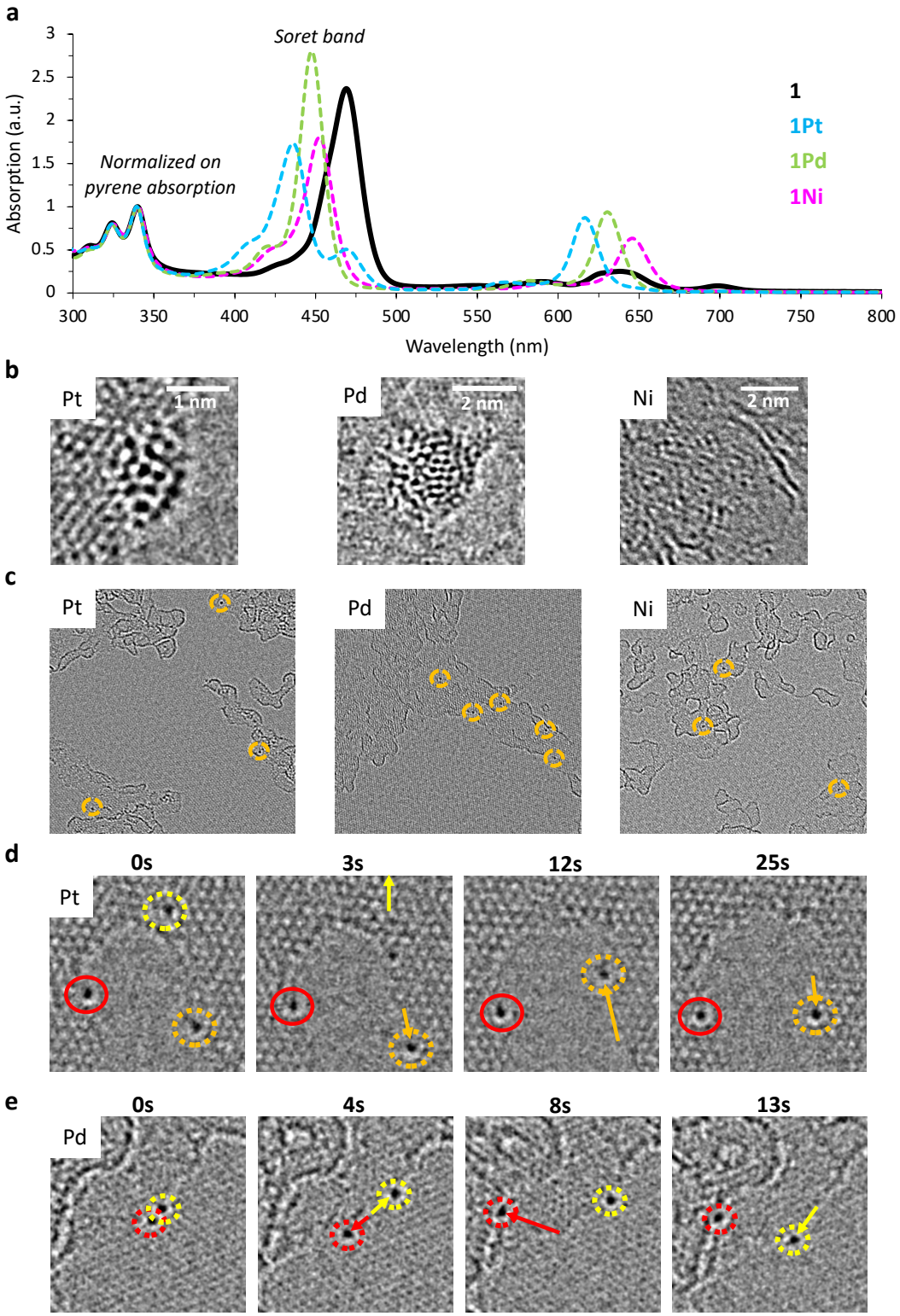

Extended Data Fig. 2. Characterization of 1M (M = Pt, Pd, Ni) species. a, UV/Vis analysis in THF at rt. Spectra are normalized at the absorption maximum of pyrene at 341 nm. **b**, TEM image of Pt, Pd, and Ni-atom aggregates. **c**, Low-mag TEM image of single metal atoms from **1M** species. **d**, Time-dependent diffusion of single Pt-atoms. **e**, Time-dependent diffusion of single Pt-atoms. Arrows indicate the direction of motion.

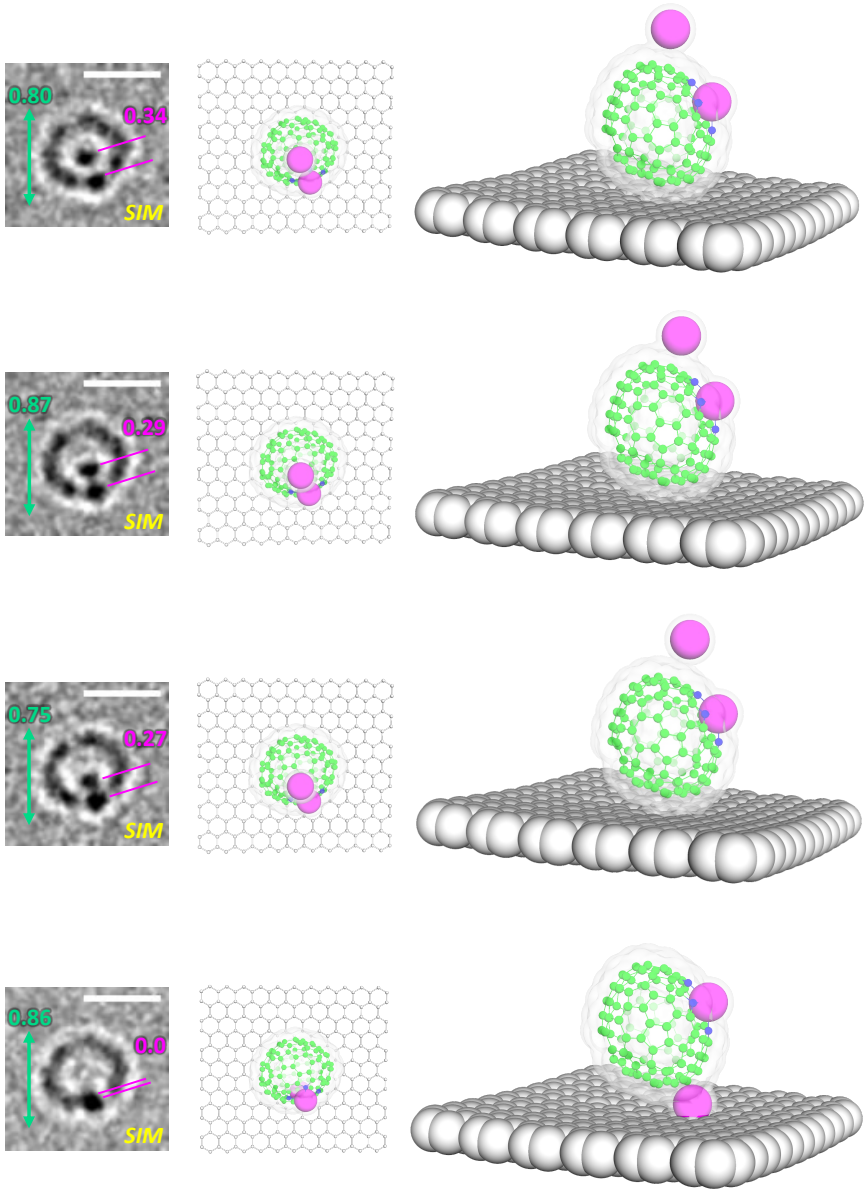

Extended Data Fig. 3. Alternative simulations with an outside bound Pb atom instead of an endohedral metal atom. The surface of the molecule displays the van der Waals surface. In the side view, the graphene is depicted as a CPK model. Scale bar 1 nm.

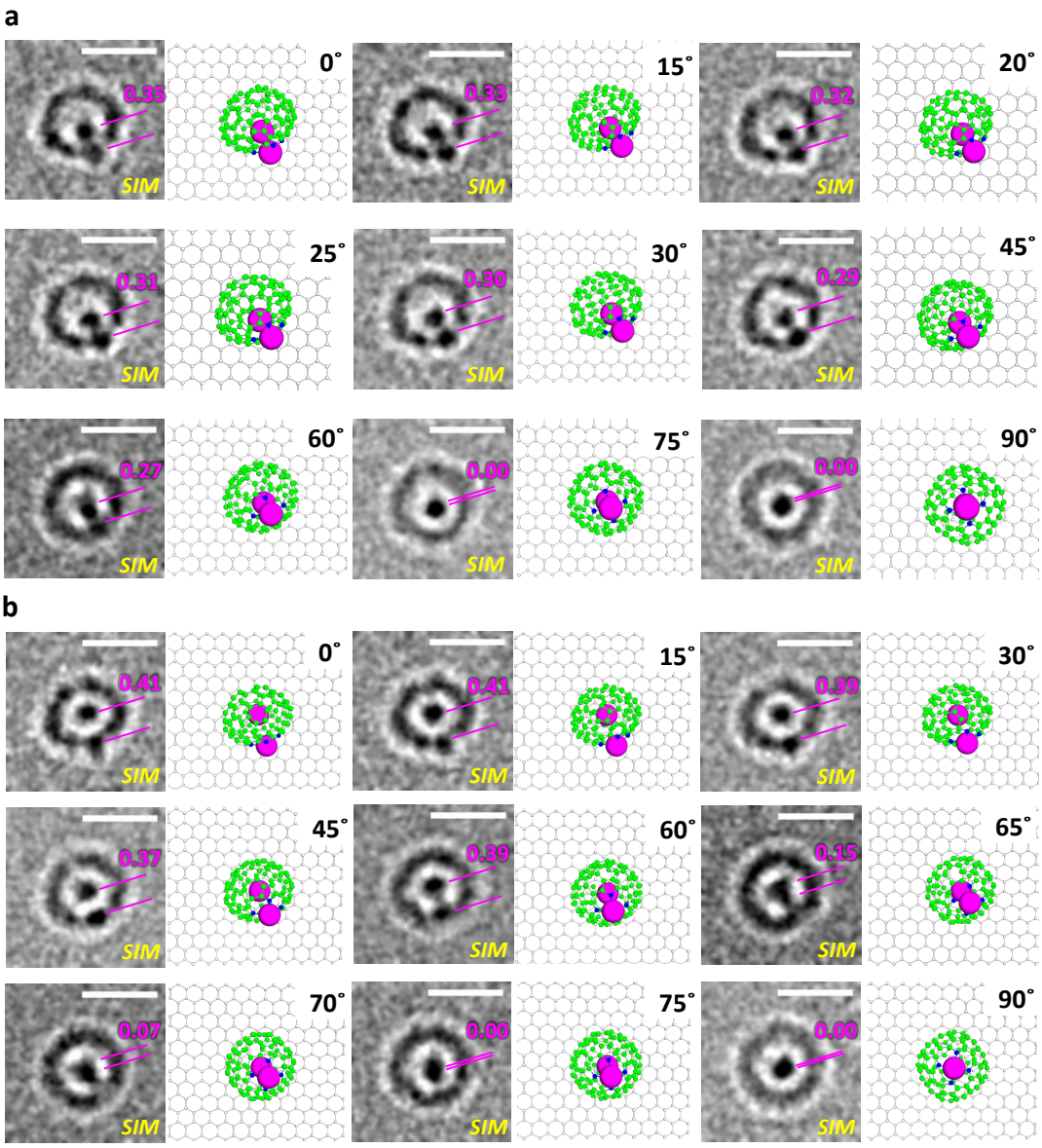

Extended Data Fig. 4. Simulation analysis of Pb-Pb distance in Pb@(FP-Pb) at various tilting angles. The measured angle is derived from the static graphene surface and the tilted molecule along the Pb-Pb bond. **a**, Pb-Pb single bond. **b**, non-bonded Pb atoms. Scale bar 1 nm.

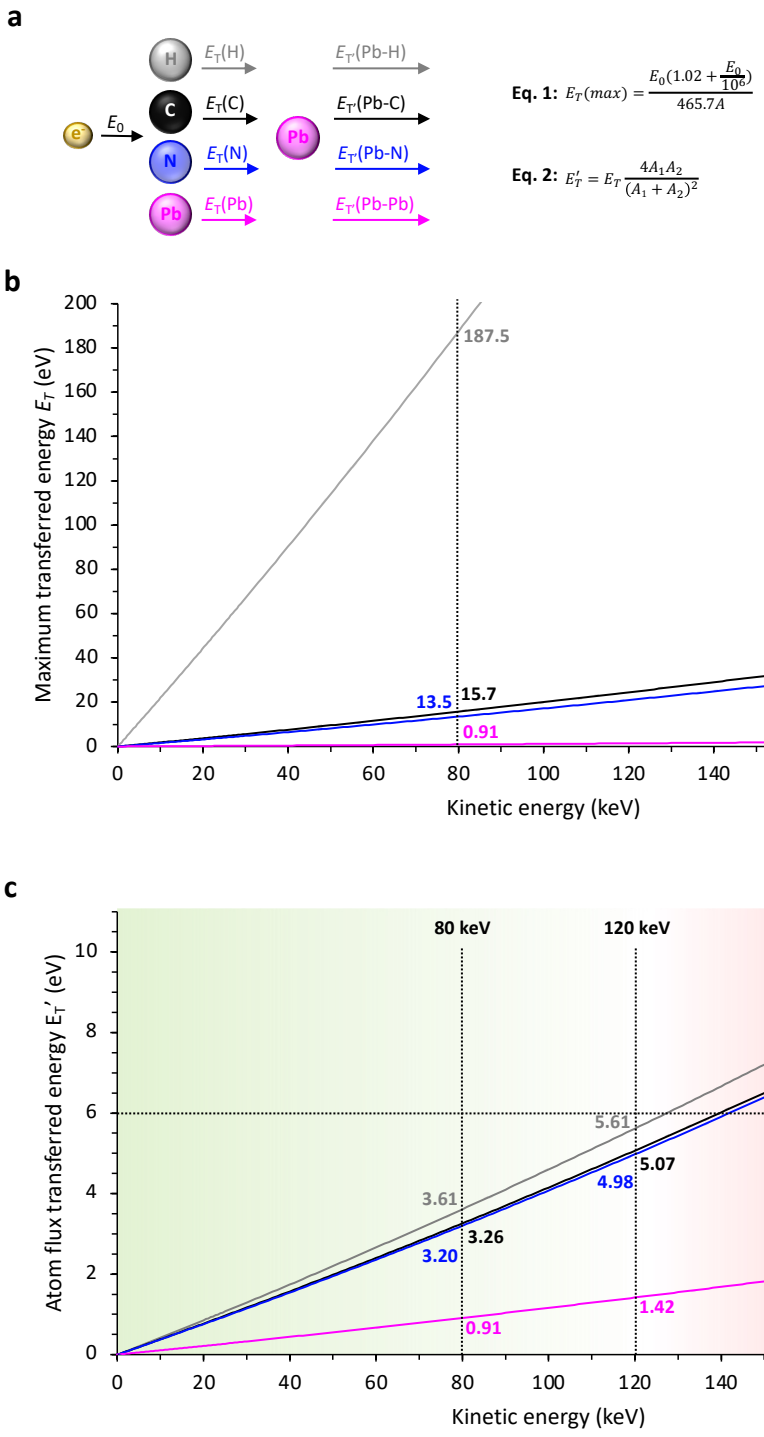

Extended Data Fig. 5. Secondary knock-on-induced demetallation of complexed Pb atoms through a fast atom flux. a, Schematic depiction of energy transfer E_T from primary electrons to atoms (H, C, N, Pb) and subsequent energy transfer $E_{T'}$ from the fast moving atoms to Pb atoms, calculated from Equation 1 and 2. **b**, Maximum transferred kinetic energy from the primary beam *via* elastic scattering against the kinetic energy of the primary electrons. **c**, Maximum transferred kinetic energy from fast atoms to Pb atoms *via* secondary knock-on energy transfer against the kinetic energy of the primary electrons.

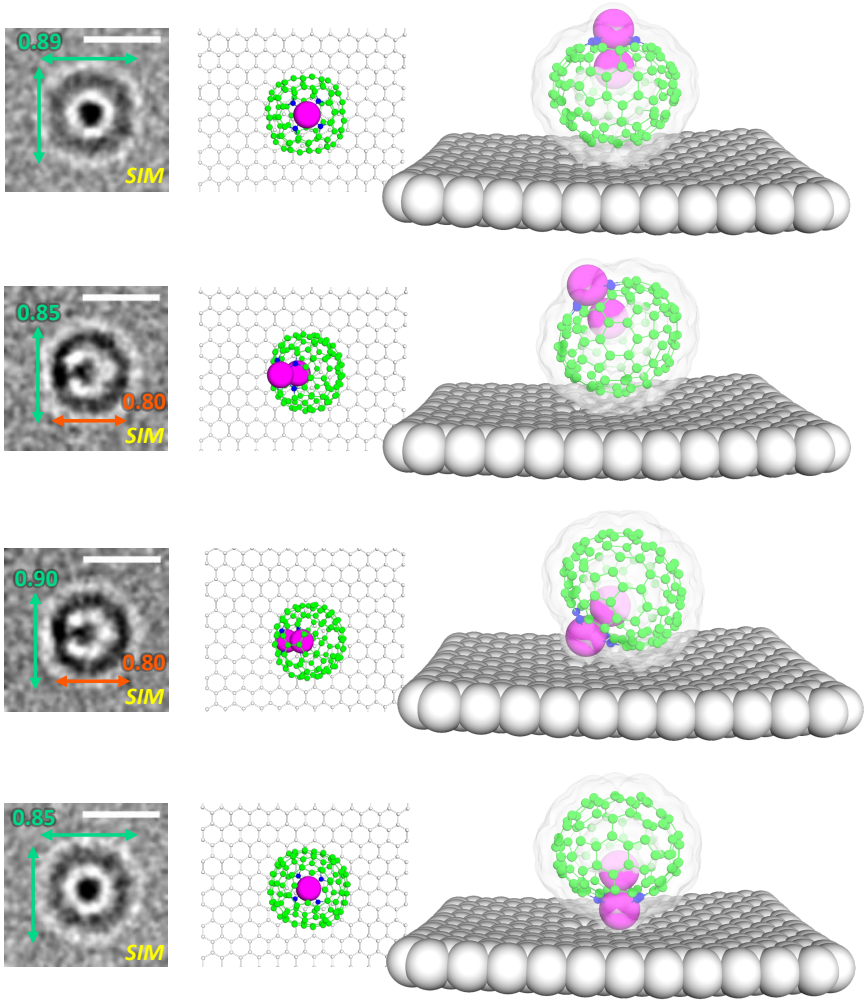

Extended Data Fig. 6. Additional simulation images of Pb@(FP-Pb) with graphene's most significant van der Waals surface interactions. Scale bar 1 nm.

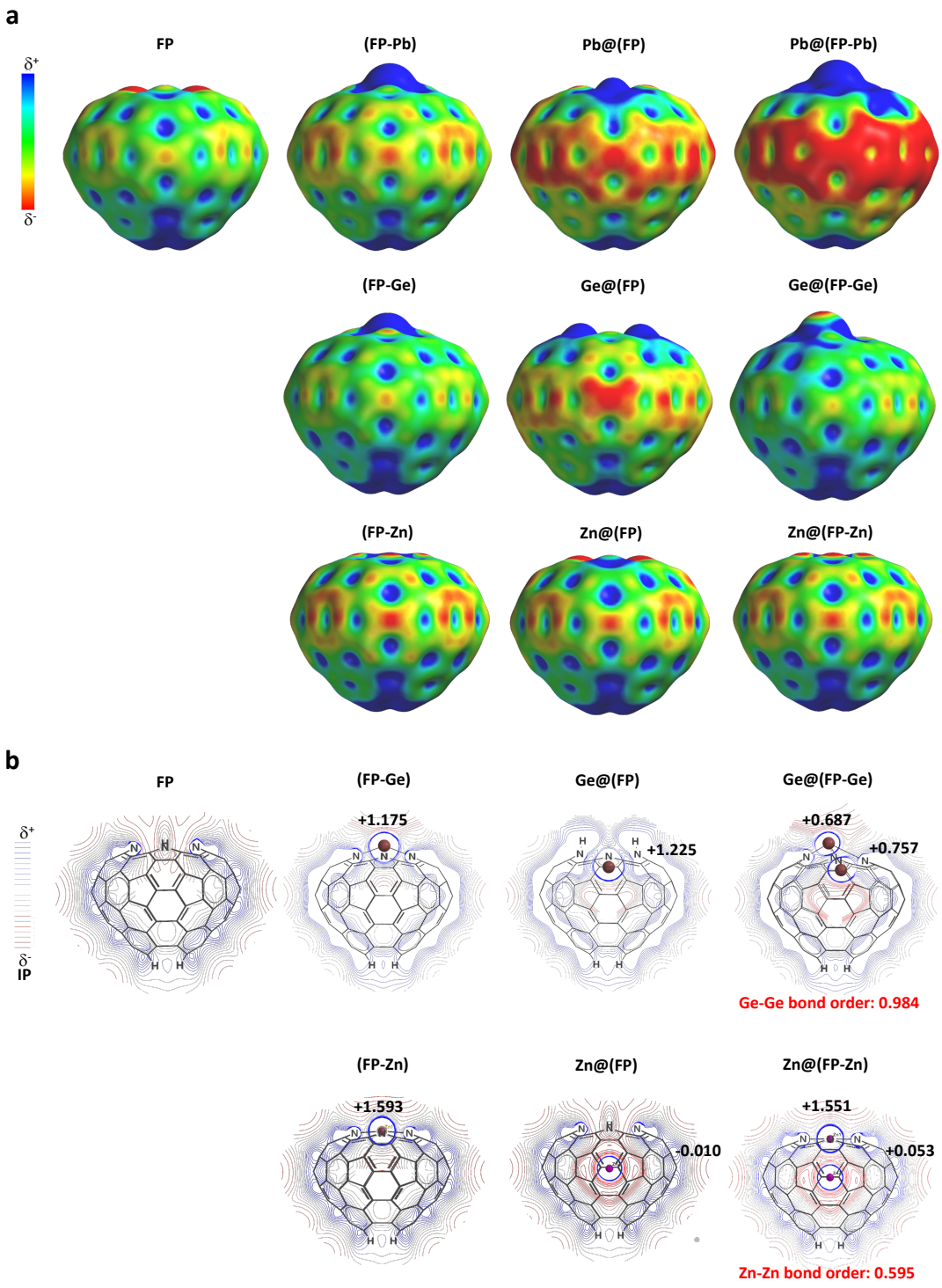

Extended Data Fig. 7. Electronic evaluation of different Pb-, Ge-, and Zn-fullerophyrins. a, Electrostatic potential map of **FP**, **(FP-M)**, **M@(FP)**, and **M@(FP-M)** (color range from -30 to +20 kJ/mol, isovalue 0.002 e/au^3) **b**, Sliced contour plot of the ionization potential of **FP**, **(FP-M)**, **M@(FP)**, and **M@(FP-M)** (color range from 7 to 15 eV). Black digits indicate natural atomic charge of metal atoms. DFT level: B3LYP-D3/6-311G(2d,p)//ωB97X-D/6-31G(d) for Zn and Ge derivatives, B3LYP-D3/6-31G(d)/LANL2DZ>Kr for Pb-derivatives.

Extended Data Table 1. Expected knock-on-induced events of 1. Summary on the threshold displacement energies E_d, the resulting displacement cross-section σ_d at 80 keV, and the minimum total electron dose TED_d for the homolytic C–H or C–C bond cleavage in **1**; calculated at the M06-2X/def2-TZVP[6-31G(d)] level of theory for C–*H*, ωB97X-D/6311G(d,p) for C–*C*, and B3LYP/6-31G(d)/LanL2DZ>Kr for C-*N*-Pb.

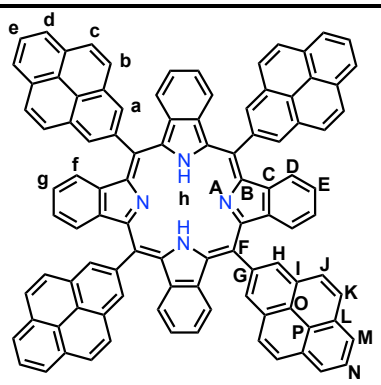

Entry	Displaced Atom	E_d (eV)[b]	σ_d (barn)	*n*	TED_d [10^6 e$^-$nm^{-2}][a]
1	a, d	7.6954	66.18	8	18.9
2	b, c	7.7200	65.96	8	19.0
3	e	7.7453	65.73	4	38.0
4	f	7.7305	65.86	8	19.0
5	g	7.7955	65.28	8	19.1
6	h	6.0747	85.07	2	58.8
7	A	12.9476	4.51	4	554
8[b]	B	14.7910	5.07	8	247
9[b]	C	15.9183	0	8	∞
10[b]	D	12.5106	21.14	8	59.1
11[b]	E	12.4076	22.03	8	56.7
12[b]	F	15.5115	1.13	4	2212
13[b]	G	16.2214	0	4	∞
14[b]	H	11.8299	27.34	8	45.7
15[b]	I	16.5368	0	8	∞
16[b]	J	11.9548	26.14	8	47.8
17[b]	K	11.9564	26.13	8	47.8
18[b]	L	16.5063	0	8	∞
19[b]	M	12.0643	25.12	8	49.8
20[b]	N	12.7094	19.48	4	128
21[b]	O	16.4954	0	4	∞
22[b]	P	16.7263	0	4	∞

[a] assuming an isotropic energy transfer for all H atoms (implying fourfold symmetry).
[b] E_d approximated from E_{BDE} for C-*C* cleavage.